POLITECNICO DI TORINO

KTH Royal Institute of Technology

Master's Degree in Materials Engineering

Master's Degree Thesis

Alternative binders for cemented carbides

A study on the influence of carbon content and sintering conditions on microstructure and properties

Supervisors:	Candidate:
PhD Ida BORGH	Luca DELTETTO
PhD Stella STEN	Examiner:
Prof. Milena SALVO	Prof. Mikael HEDENQVIST

Academic Year 2025-2026

Alternative binders for cemented carbides

Luca Deltetto

Abstract

Cemented carbides are composite materials traditionally made of tungsten carbide (WC) and cobalt (Co). The former, referred to as the hard phase, provides hardness, while the latter is the binder and provides toughness. This combination of properties makes cemented carbide suitable for applications such as rock drilling or metal cutting. Since Co is classified as a critical raw material by European Union, and recent studies find out that is dangerous for human health, this research investigates an alternative binder system for WC cemented carbides as a potential substitute for Co. The focus is put on a system based on Iron, Nickel and Co, with a ratio of 50-25-25 wt%. In particular, the study examines how variations in carbon content and sintering temperature influence microstructure and mechanical properties of the material.

Thermodynamic calculations predict a narrow equilibrium carbon window; however, a twice as large carbon window is experimentally verified, after normal powder metallurgy production. By systematically varying carbon content, all the possible structures were mapped, from η-phase formation at low carbon levels to graphite precipitation at high levels. Three compositions were identified to have a stable two-phase WC-binder structure.

Magnetic measurement can be obtained for the investigated binder composition; however, no clear trends are observed within the two-phase region.

Electron Back-Scattered Diffraction (EBSD) analysis revealed that carbon content do not significantly affect the WC grain size or grain size distribution. Higher sintering temperature, however, resulted in a coarser upper tail of the WC grain size distribution compared to the lower temperature. The EBSD analysis also showed that the binder phase structure after sintering is predominantly austenitic.

Mechanical testing showed that hardness stayed constant within the two-phase region, while fracture toughness increased with carbon content. Wear test demonstrated a difference in performance depending on C content.

These findings confirm that carbon balance and sintering temperature are important to consider when using alternative binders for cemented carbides.

Alternativa bindemedel för hårdmetall

Luca Deltetto

Sammanfattning

Hårdmetall är ett komposit material som traditionellt består av volframkar- bid (WC) och kobolt (Co). Den förstnämnda, kallad för en hård fas och ger materialet dess hårdhet, medan den sistnämnda fungerar som ett bindefas och ger materialet dess seghet. Denna kombination av egenskaper gör hårdmetall lämplig för applikationer som bergborrning eller skärande bearbetning. Co är idag klassificerat som ett kritiskt råmaterial av Europeiska unionen. Nyare studier har visat på att Co kan ge vissa hälsorisker. Därför undersöker denna studie ett alternativt bindefassystem för hårdmetaller, som en potentiell ersättning för Co. Fokus ligger på ett system baserat på järn (Fe), nickel (Ni) och kobolt (Co) med ett förhållande på 50-25-25 viktprocent. Studien undersöker särskilt hur variationer i kolhalt och sintringstemperatur påverkar mikrostruktur och mekaniska egenskaper.

Termodynamiska beräkningar förutsade ett smalt möjligt kolintervall vid jämnvikt för denna alternative legering, vilket bekräftades experimentellt. Genom systematiska variationer av kolhalten har möjliga strukturer, från η-fasbildning vid låga kolhalter till grafitutfällning vid höga kolhalter kartlagds. Tre sammansättningar identifierades ha en stabil tvåfasstruktur med WC-bindfas.

Magnetiska mätningar (koercivitet och Co-magnetism%) ger utslag för den undersökta sammansättningen men visar ingen klar trend för proverna inom tvåfasområdet. Electron Back-Scattered Diffraction (EBSD)-analys visade att kolhalten inte påverkar WC kornstorleken eller kornstorleksfördelningen nämnvärt. En högre sintringstemperatur resulterade däremot i en grövre övre svans i kornstorleksfördelningen jämfört med den lägre temperaturen. EBSD-analysen visade också att bindefasens struktur efter sintring huvudsakligen är austenitisk.

Mekaniska tester visade att hårdheten är konstant inom tvåfasområdet, medan segheten ökade med kolhalten. Ett slitagetestet visade en skillnad i prestanda beroende på C halt.

Resultaten från denna studie bekräftar att kolbalans och sintringstemperatur är viktiga faktorer att ta hänsyn till när alternativa bindefaser för hårdmetall används.

Acknowledgements

An incredible journey is coming to an end, and I would like to thank all the people who have been part of it.
I would like to express my sincere thanks to Ida and Stella for guiding, inspiring, and helping me throughout this project.
I am grateful to all my colleagues in the R&D Rock Tool Division team. I had fun, and I felt like part of the team from the very first day. A special mention goes to Eddie, who taught me and assisted me with the lab work.
Thanks to all my friends who, in one way or another, have supported and helped me over the years. A special thanks to the new ones, who encouraged me during these last months. I am feeling so lucky to have met all of you, and having you at my side.
To Sofia, this result has also been achieved thanks to your love and support.
To my brothers, Dav and Lore, who are a daily source of inspiration and an example to follow.
To Ma and Pa, thank you for understanding me, and for supporting me in all my decisions.
Grazie!

Table of Contents

1 Introduction **1**

1.1 History and context 1
1.2 What are cemented carbides used for? 2
1.3 Aim and Objectives 3
1.4 Research questions 3

2 Cemented Carbides: an overview **4**

2.1 Production process 4
2.1.1 Powders 4
2.1.2 Mixing and milling 4
2.1.3 Drying 5
2.1.4 Pressing 6
2.1.5 Sintering and densification process 6
2.1.6 Post treatments, finishing and coatings 7
2.2 WC-Co systems 8
2.2.1 WC: the hard phase 9
2.2.2 Co: the binder 10
2.2.3 Carbon influence and carbon window 11
2.2.4 Additives 11
2.3 Alternative binders 12
2.3.1 Fe 12
2.3.2 Ni 13
2.3.3 Fe-Ni-Co systems 14
2.4 WC-50Fe-25Ni-25Co 15

3 Methodology **17**

3.1 Theoretical calculations and modeling 17
3.2 Magnetic properties 17
3.3 Density 19
3.4 Chemical analysis 19
3.5 Light Optical Microscopy 19
3.6 Stereo Microscope 20
3.7 Scanning Electron Microscope 20
3.7.1 Secondary electrons and back-scattered electrons imaging . . 21

3.7.2 Energy Dispersive Spectroscopy . . . 21
3.7.3 Electron Back-Scattered Diffraction . . . 22
3.8 Mechanical characterization . . . 23
3.8.1 Hardness . . . 23
3.8.2 Fracture toughness and Palmqvist method . . . 23
3.8.3 Wear test . . . 24
3.8.4 Crush test . . . 25

4 Experimental details 26
4.1 Calculations . . . 26
4.2 Materials . . . 27
4.3 Samples manufacturing . . . 27
4.3.1 Milling and Drying . . . 27
4.3.2 Pressing and Sintering . . . 28
4.3.3 Post treatment . . . 28
4.4 Sample preparation . . . 29
4.5 Properties measurements . . . 29
4.5.1 Hc, Com% and density . . . 29
4.5.2 Hardness and Toughness . . . 30
4.5.3 Wear and Crush . . . 31
4.6 Microscopy for structure characterization . . . 31
4.6.1 Structure evaluation and overview imaging . . . 31
4.6.2 Image Analysis . . . 32
4.6.2.1 Binder phase quantification . . . 32
4.6.2.2 Binder phase grain size . . . 32
4.6.3 Detailed structure analysis for the two-phase materials . . . 33

5 Results and Discussion 35
5.1 Structure overview and basic properties . . . 35
5.2 Chemical Analysis . . . 40
5.3 Detailed structure analysis using EDS and EBSD . . . 42
5.3.1 Phase fraction . . . 42
5.3.2 WC grain size and distribution . . . 43
5.3.3 True binder grain size evaluation . . . 48
5.4 Testing of inserts . . . 50
5.4.1 Material selection and evaluation . . . 50
5.4.2 Effect of post treatment . . . 53
5.4.3 Wear test . . . 55
5.4.4 Crush test . . . 56
5.5 Hc, WC grain size and hardness relation . . . 57

6 Conclusions 60
6.1 Future work . . . 61

Bibliography **62**

A Appendix A **72**

B Appendix B **75**

C Appendix C **78**

C.1 Hc: comparison between different sintering trials 78

List of Figures

1.1 Ideal tool material graph. Freely after [13]. 2

2.1 Scheme representing the main steps for the production of cemented carbides. [18] 5
2.2 Typical sintering cycle for cemented carbides. Adapted from [24] . . 6
2.3 Liquid phase sintering stages. [26] 7
2.4 Relation between WC grain size and binder content with main properties of cemented carbides. [14] 8
2.5 Mechanical properties of different WC-Co grades. A: Hardness vs %wtCo. B: Fracture toughness vs %wtCo. Adapted from [32]. 9
2.6 A: WC crystal structure. Adapted from [39]. B: WC crystal shape. Adapted from [40]. 10
2.7 WC-Co isopleth [46]. 11
2.8 WC-Fe isopleth [46]. 13
2.9 WC-Ni isopleth [46]. 14
2.10 WC-Fe-Ni-Co isopleth [46]. 16

3.1 Relationship between coercivity (Hc), magnetic saturation (M_S) and the microstructure of cemented carbides. Image from [14]. 19
3.2 LOM micrographs 20
3.3 Interaction volume [70]. 21
3.4 The emission mechanisms for SE, BSE and X-rays. [70] 22
3.5 The EBSD hardware setup inside an SEM. [75] 23
3.6 Cracks length measurement through LOM picture 24
3.7 Cross section of the schematic setup for the rock turning wear test. The sample moves from the long axis of the rock cylinder. Adapted from [79]. 25

4.1 Phase diagram of the selected material, calculated with ThermoCalc and the TCFE13 database [46]. 27
4.2 Ion beam polishing scheme. θ represents the angle. 30
4.3 Image analysis. 32

5.1 Density vs C content. The squares highlight the samples having the two-phase structure. 36

5.2 Hc vs C content. The squares highlight the samples having the two-phase structure. 37
5.3 Com% vs C content. The squares highlight the samples having the two-phase structure. 38
5.4 HV20 vs C content. The squares highlight the samples having the two-phase structure. Further details presented in Table A.1 in Appendix A. 38
5.5 Palmqvist toughness (normalized) vs C content. The squares highlight the samples having the two-phase structure. Further details presented in Table A.2 in Appendix A. 39
5.6 HV20 vs Palmqvist toughness (normalized). The squares highlight the samples having the two-phase structure. 40
5.7 Analyzed C content for the different C levels. The square highlights the samples having the two-phase structure. 41
5.8 Analyzed (Real) metallic binder elements composition using XRF and nominal (Th) composition vs C content. 41
5.9 WC relative area based grain size distribution for 1410°C (left) and 1500°C (right) sintering. Colors follow increasing carbon content: blue, yellow, red for 1410°C; red, blue, yellow for 1500°C. 44
5.10 WC Nordgren size distribution for 1410°C (left) and 1500°C (right) sintering. Colors follow increasing C content: blue, yellow, red for 1410°C; red, blue, yellow for 1500°C. 44
5.11 EBSD maps colored based on ECD. Comparison between WC grain size. Left: 1410°C samples; 02_02 (top), 10_02 (center), 03_02 (bottom). Right: 1500°C samples; 09_03 (top), 02_03 (center), 10_03 (bottom) 46
5.12 EBSD maps coloreed by inverse pole figure (orientation) for the binder phase grains. Comparison between binder phase grain size. Left: 1410°C samples; 02_02 (top), 10_02 (center), 03_02 (bottom). Right: 1500°C samples; 09_03 (top), 02_03 (center), 10_03 (bottom) . . . 49
5.13 Density vs C content for the insert samples. 51
5.14 Hc vs C content for the inserts samples. 52
5.15 Co-m% vs C content for the inserts samples. 52
5.16 Example of hardness distribution map, program P5. The color scale indicates hardness difference across the section. 54
5.17 Wear test result: Average volume loss vs C level. 55
5.18 Stereo micrographs of the tips from samples exposed to wear test. Left: 10_02_i; right: 10_03_i. 56
5.19 Crush test result: Fracture energy vs C level. 57
5.20 Relation between Hc, WC grain size (expressed as D50) and C content, for 1410°C samples. 58
5.21 Relation between Hc, WC grain size (expressed as D50) and C content, for 1500°C samples. 58

B.1 Observed structures. First row: on the left η-phase in yellow; on the right two-phase structure. Second row: flaked graphite (left) and nodular graphite (right). 75
B.2 Magnetic saturation (Ms) vs C content 76
B.3 Comparison between WC cumulative curves. Left: 1410°C samples; 02_02 (top), 10_02 (center), 03_02 (bottom). Right: 1500°C samples; 09_03 (top), 02_03 (center), 10_03 (bottom) 76
B.4 True binder grain maps for 1410°C samples: 02_02 (top), 10_02 (center), 03_02 (bottom). 77

C.1 Hc vs C content: comparison between inserts and SNUNs. 78

List of Tables

4.1 Samples series 28
4.2 Ion beam polishing steps. 29
4.3 Post-treatment programs associated with sample 02_02_i. 30
4.4 BSE and EDS settings details. WD is the Working Distance. 33
4.5 Instrument, analysis, and post-processing settings 34

5.1 Observed structure for the SNUN samples. 35
5.2 Control samples: density, coercivity, and magnetic saturation. 36
5.3 Normalized phase fraction for 1410°C and 1500°C samples. Normalization against the sample with the lowest C content for each sintering. 42
5.4 Normalized comparison of ImageJ, EBSD and EDS (both flat and tilted) binder phase fraction (%) for 1410°C and 1500°C samples. . . 43
5.5 WC grain size statistic values for 1410°C abd 1500°C samples.. . . . 45
5.6 Comparison of ImageJ count, Hand count, ECD (Equivalent Circle Diameter), and LIM (Linear Intercepts Method) for 1410°C and 1500°C samples. ECD and LIM are expressed in [μm]. 48
5.7 Observed structure for the inserts samples. 50
5.8 Control samples for the sintering of the inserts: density, coercivity, and magnetic saturation. 53
5.9 Hardness change between surface and bulk. Same composition, different treatment. 54
5.10 Wear scars measurements and calculations with standard deviation. 56
5.11 Example of calculation of Hall-Petch WC grain size contribution for 1410°C samples. 59

A.1 Hardness values with standard deviation. 72
A.2 Toughness values with standard deviation. 73
A.3 Average density and standard deviation for the inserts sintered at different temperatures. 73
A.4 Average coercivity (Hc) with standard deviation. 73
A.5 Average Co-m% with standard deviation. 74
A.6 Average volume loss per turning distance [mm^3/m] and standard deviation from the wear test. 74
A.7 Average fracture energy [J] and standard deviation. 74

Acronyms

BSE	Back Scattered Electron.
CALPHAD	CAlculations of PHAse Diagrams.
CIP	Cold Isostatic Pressing.
CVD	Chemical Vapor Deposition.
EBSD	Electron Back-Scattered Diffraction.
ECHA	European Chemical Agency.
ECD	Equivalent Circle Diameter.
EDS	Energy Dispersive Spectroscopy.
ICME	Integrated Computational Materials Engineering.
ISO	International Organization for Standardization.
LIM	Linear Intercept Method.
LOM	Light Optical Microscopy.
PEG	Polyethylene glycol.
PVD	Physical Vapor Deposition.
SE	Secondary Electron.
SEM	Scanning Electron Microscope.
XRF	X-ray fluorescence.
bcc	body centered cubic.
fcc	face centered cubic.
hcp	hexagonal closed-packed.

Chapter 1

Introduction

1.1 History and context

Cemented carbides have a long history, and their initial use was different from what we know today. Tungsten carbide (WC) was first synthesized by Henri Moissan, a French chemist who was investigating the synthesis of new refractory compounds. The production of WC-based cemented carbides started in the companies producing tungsten powders for the fabrication of tungsten wires, which were used as filaments for electrical lighting [1]. The aim of these companies was to develop new hard materials to replace the diamond dies needed to draw tungsten wires. Intensive studies were carried out in several different German companies when in 1923 Karl Schröter, employed at OSRAM, filed a patent for a WC-Cobalt (Co) material. OSRAM did not intend to widen the application and instead offered the patent to the Krupp Company, which decided to start a small production of the new material. In 1927, the first Krupp's WC-Co cutting tool was presented, with the name WIDIA, from German "WIe DIAmant" ("like diamond") [2]. Since then, different cemented carbides have been used as cutting and drilling tools and still play an important role in modern industries all over the world.

Hardmetals is the term now used to describe this class of materials, which consist of a hard refractory carbide, nitride, or carbonitride of a transition metal embedded in a metal binder matrix. Nowadays there are multiple different grades available on the market, depending on the properties needed for the specific application. Usually, when cemented carbides are mentioned, WC-Co systems are meant, while cermets refers to Ti(C,N) based materials [3]. Hardmetals are composite materials that combine the physical properties of ceramics (i.e., hardness, strength) with the mechanical and electronic properties of metals (i.e., ductility and toughness; high thermal and electronic conductivity) [4]. In material science, hardness (usually intended as the ability to withstand localized plastic deformation [5]) and toughness (the ability to absorb energy and plastically deform without fracturing [6]) are two competing properties: a material is usually hard and brittle or tough and soft. As shown in Figure 1.1, the extremely hard diamond is brittle, while high-speed steels (HSS) are tough but lack in hardness. Cemented carbides are located almost in the center of

this graph, where a trade off between the hard ceramic particle and the metal binder toughness can be found.
Despite the great variety of hardmetals that can be used, WC-Co is still the most successful combination due to the wettability of WC by Co during sintering, leading to higher densification and higher toughness [7]. It would appear that Co is the perfect binder, but unfortunately, it has relevant drawbacks. Indeed, as shown by different studies, there are health risks [8] associated with WC-Co inhalation [9], as well as contact with human cells [10]. Furthermore, Co is listed as a critical raw material (the list of materials that are economically and strategically important for the European economy and have a high risk associated with their supply) [11] and according to the European Chemical Agency (ECHA) Co is classified as a toxic substance [12]. For these reasons, new binders have been explored since the 1980s, with the greatest interest focused on iron (Fe) and nickel (Ni) and their alloys, since they are the closest transition metals to Co in the periodic table and they are expected to have similar affinity to carbon (C) and tungsten (W) as Co.

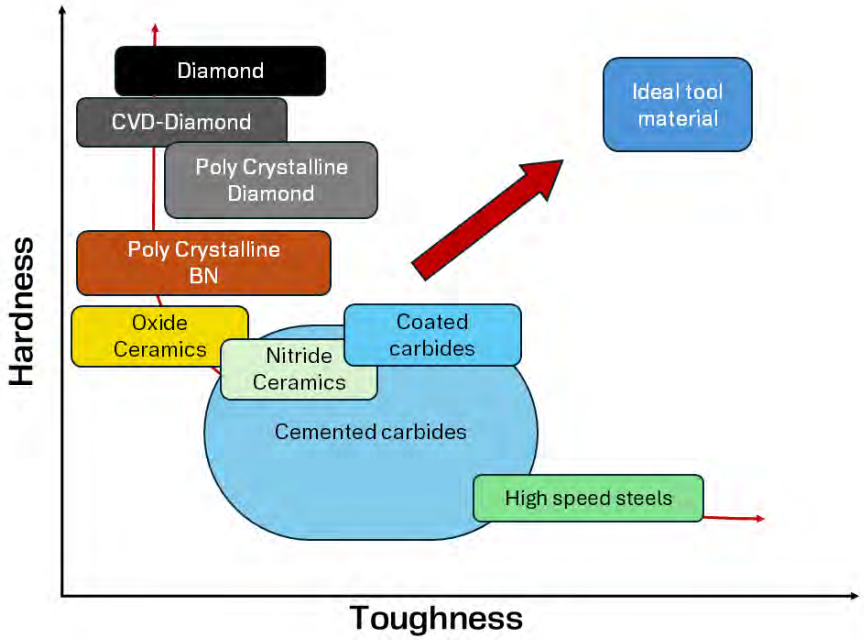

Figure 1.1: Ideal tool material graph. Freely after [13].

1.2 What are cemented carbides used for?

In the last 30 years, the global production of cemented carbides has grown significantly, especially due to the increase in production by China (28000 tons produced in 2017). Cemented carbides make up 50% of the world's hard material market. Today, almost 65% of the total production of cemented carbides is related to cutting tools, while the mining and rock industry holds approximately 15% of the market. Wood and construction industries account for 10% [14]. All of these applications place high demand on the performance of the material.

Cutting tools are used for metal cutting, which is the most important process in metalworking. This operation involves high temperatures, pressure, and wear. To survive in this environment, the tool is made of a cemented carbide substrate and a coating. The former gives hardness, compressive strength, and heat conductivity; the latter (usually a few μm thick layer of Ti(C,N) or Al_2O_3) provides wear resistance [15].
In case of rock drilling, cemented carbide inserts are inserted into a steel body. Depending on the type of drilling (e.g. percussive, rotary, or cutting), the inserts are exposed to different load conditions and therefore require different properties. For all of them, a sufficiently high fracture toughness is needed to slow down crack propagation and to avoid total failure. In general, a compromise must be found between hardness (and therefore wear resistance), compressive strength, and fracture toughness [16].

1.3 Aim and Objectives

The objective of this thesis is to explore an alternative binder system for WC cemented carbides, specifically one based on Fe, Ni, and Co, and to examine how variations in C content influence the resulting microstructure and material properties. The composition studied is based on the work of Prakash, in which the binder consists of Fe, Ni, and Co in a 50/25/25 %wt ratio [17]. Keeping the binder content constant, the C content is systematically increased across different samples to assess its impact on both structure and performance.
In addition, the influence of the sintering temperature on structure and properties is also investigated.
This work is carried out at Sandvik Mining, in the R&D Rock Tools Division.

1.4 Research questions

- What is the effect of C content on the microstructure and properties of cemented carbides with an alternative binder consisting of Fe, Ni and Co in a 50/25/25%wt ratio?
- How does sintering temperature affect the microstructure and properties for this material?

Chapter 2

Cemented Carbides: an overview

This chapter presents the state of the art of cemented carbides, providing an overview from the production process to current material innovations.

2.1 Production process

The production of cemented carbides follows a complex powder metallurgy route (Figure 2.1), involving steps such as raw powder production, mixing and milling of powders, drying, pressing to final shape, and sintering. All of these manufacturing steps are linked, meaning that any change in any of them will influence the next. Furthermore, the whole process affects the microstructure of the final product and therefore its properties.

2.1.1 Powders

The powder raw materials are available in the market as commercial products and their selection is the first stage in the manufacturing of cemented carbides. This selection is critical to achieve the quality in the final sintered product. Composition, particle size, morphology, and surface chemistry are the parameters that determine the quality of the powders.
The primary sources of tungsten are the minerals Scheelite ($CaWO_4$) and Wolframite $(Fe,Mn)WO_4$, where the tungsten is extracted through a hydrometallurgical process, which result is WO_3, then carburized to WC by hydrogen reduction [19]. Because of the limited availability of Co ores, Co is primarily produced as a by-product of more abundant metals such as copper (Cu) and Ni, or it is recovered through the chemical recycling of cemented carbide scrap. Pure Co is then extracted by hydrometallurgical processing of these sources [20].

2.1.2 Mixing and milling

Usually, milling is conducted in a cylindrical rotating mill, and WC-Co balls are used as milling bodies. Once the tungsten carbide and metal binder powders are available, they are mixed together with a polymeric pressing agent, for instance wax,

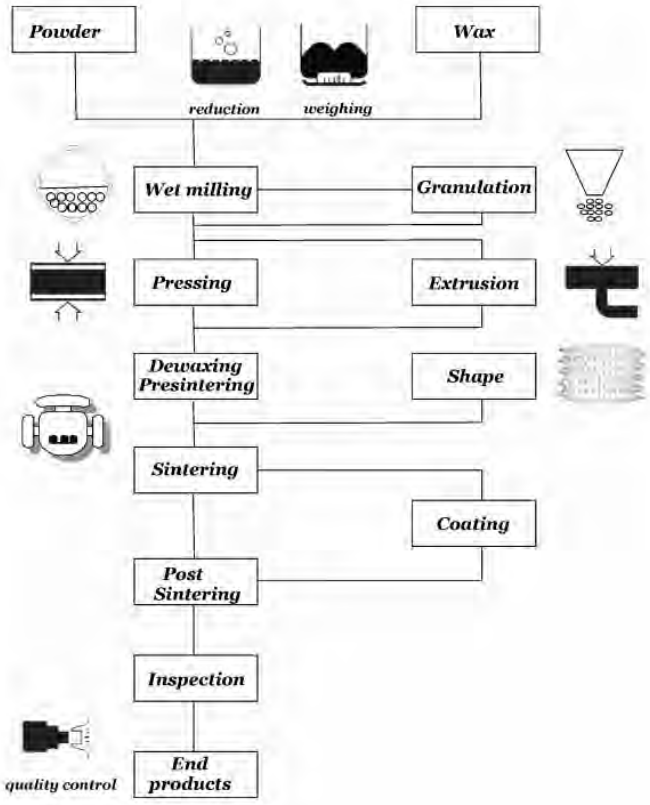

Figure 2.1: Scheme representing the main steps for the production of cemented carbides. [18]

and a milling liquid or solvent, i.e. usually ethanol, to prevent oxidation. The aim of this step is to reduce particle size and their distribution, and obtain a homogeneous blend, sometimes referred to as slurry. The milling time is related to the particle size distribution and, in general, the longer the time, the smaller the particles and the more homogeneous their distribution. Moreover, this will affect the final grain size distribution of WC [18].

2.1.3 Drying

After milling, the powders are dried. To do so, the commonly used technique is spray drying, which consists of transforming a liquid feed into a dry powder by rapidly drying it with a hot gas. The slurry containing powders, pressing agent, and solvent is passed from the feed tank to the drying chamber by applying pressure through a nozzle. The chamber is usually heated by a gas blown in from the bottom. Due to surface tension forces, the sprayed liquid in the gas assumes a spherical shape. Since the gas temperature is around 200°C, the solvent evaporates in contact with the gas, leading to the formation of dried spherical granules [21]. Spray drying is preferred to vacuum drying and granulation because lubricant is greatly homogenized as a result of constant agitation of the slurry and its instant drying. Furthermore, spray dried powders are typically nearly spherical and relatively coarse, characteristics

that improve flowability and packing behavior, both of which are essential to achieve high-quality pressing [22].

2.1.4 Pressing

The dried powders are then pressed to obtain the so-called *green body*. Pressing is a very important step because it determines the quality and geometry of the final product [22]. Normally, compaction is performed by uniaxial pressing, but cold isostatic pressing (CIP) [23], extrusion and injection molding are also commonly used [21]. The obtained green body contains the binder agent and pores, which are removed during sintering [18].

2.1.5 Sintering and densification process

Sintering is the step that follows pressing and aims to achieve densification of the cemented carbide product [14]. This transformation occurs at high temperatures but below the melting point of WC. A typical sintering cycle for cemented carbides is illustrated in Figure 2.2, and consists of four main stages: de-waxing (or de-binding), heating, liquid phase sintering, and cooling.

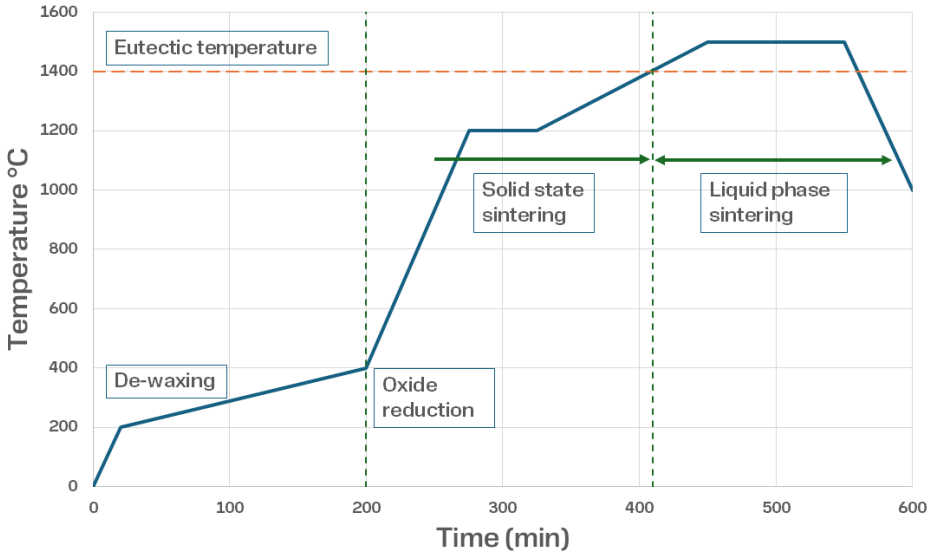

Figure 2.2: Typical sintering cycle for cemented carbides. Adapted from [24]

The initial stage, carried out at approximately 300°C, involves shrinkage due to degassing of the polymer binder, removal of impurities, and reduction of oxides [25]. According to Figure 2.3, at this stage, the material is a mixture of powders and pores between the particles. As the temperature increases, the second stage begins, initiating solid-state sintering, while the reduction of oxides continues. The thermal energy promotes diffusion and bulk transport and gradually reduces porosity. At this point, W and C start to dissolve in the binder. As the temperature gradually increases to reach the melting point of the metal binder, the process transitions into the *liquid phase sintering* stage. Unlike other sintering processes, this involves a

portion of the powder, specifically the metal binder, reaching its melting point. Here, the binder phase wets the WC grains, and capillary forces drive a rearrangement of the grains. In many cases, the reduction of porosity is facilitated by changes in grain shape, which promotes pore filling [26]. Following an Ostwald Ripening mechanism (solution-reprecipitation), the smaller grains dissolve in favor of the larger ones, leading to grain coarsening and complete densification [27]. In the final stage, the metal binder solidifies, locking the microstructure in place.

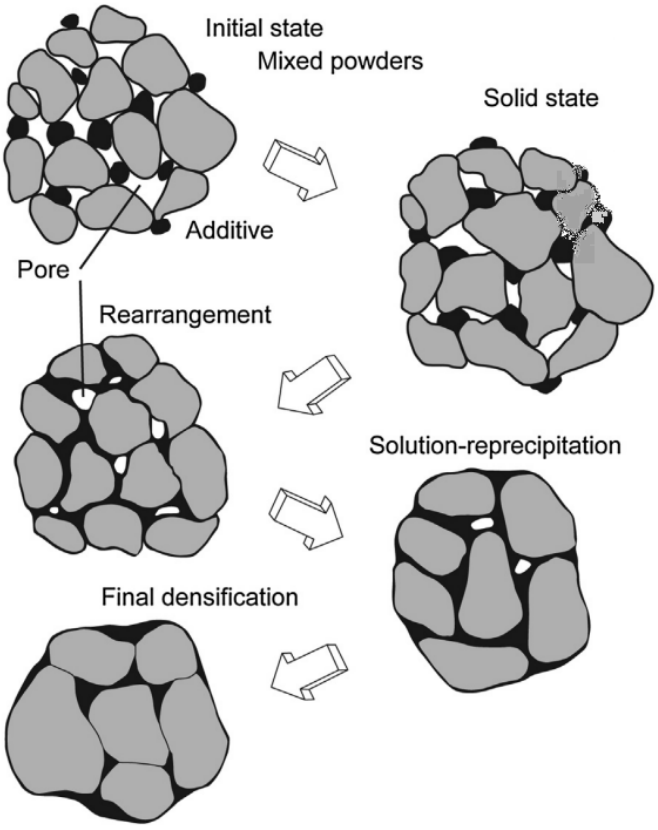

Figure 2.3: Liquid phase sintering stages. [26]

When properly conducted, the sintering process removes nearly all of the porosity, resulting in the desired mechanical and structural properties. Process parameters such as temperature, time, and atmosphere can vary depending on the chemical composition and component size.

2.1.6 Post treatments, finishing and coatings

After sintering, different post-treatments can be performed to improve some characteristics of the material. The aim is usually to improve the residual stress distribution in order to enhance fracture toughness without compromising hardness. It was demonstrated that through a number of cycles of cryogenic and heat treatment, fracture toughness can be increased by 14.3% [28]. A common post-treatment is tumbling, a mechanical surface finishing process designed to enhance both smoothness and

cleanliness. By removing burrs, scale, oxide layers, and other surface irregularities, tumbling produces a cleaner, smoother, and even surface-hardened finish. Tumbling is carried out in a barrel filled with cemented carbide abrasive components and an anti-corrosive lubricant [29]. Depending on the application, but mainly in the case of cutting tools, cemented carbides are coated after sintering, to enhance tool life and operational efficiency. The main techniques used are PVD and CVD of high hardness and high wear-resistant materials [30].

2.2 WC-Co systems

The microstructure plays a fundamental role in determining the properties of the material since they depend on the composition, fraction, and distribution of the constituent phases. WC, which serves as the hard phase, is typically stoichiometric, meaning that the binder phase does not dissolve in its crystal structure. The binder instead always has some of the carbide phase in solution. In the case of WC-Co, the Co binder phase is an alloy of Co, W, and C [31].
As mentioned, the most common system is WC-Co, which comes in various grades depending on WC grain size and Co content. By adjusting these two parameters, properties such as hardness and toughness can be tailored to specific requirements, as shown in Figure 2.4.

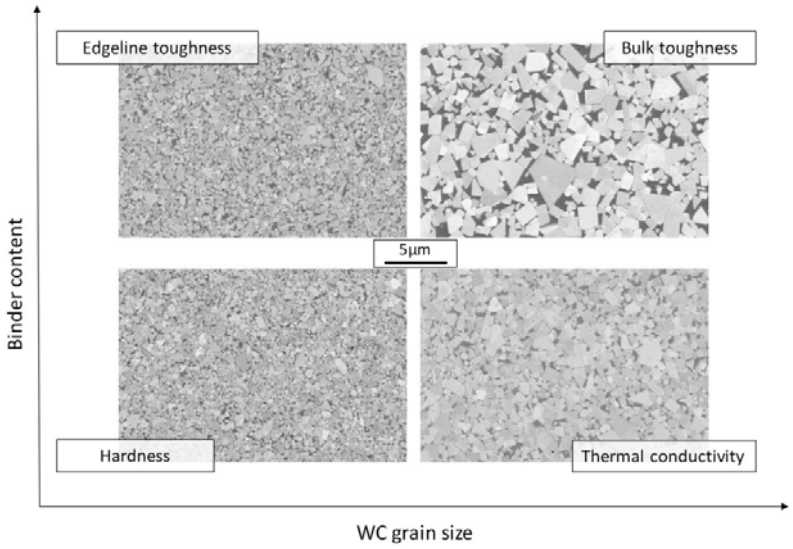

Figure 2.4: Relation between WC grain size and binder content with main properties of cemented carbides. [14]

Based on the grain size of WC, in accordance with the ISO standard, WC-Co cemented carbides are categorized into distinct groups:

- nano: $<0.2\mu$m;
- ultrafine: 0.2-0.5μm;
- submicron: 0.5-0.8μm;

- fine-grain: 0.8-1.3μm;
- medium-grain: 1.3-2.5μm;
- coarse-grain: 2.5-6.0μm;
- ultracoarse: >6.0μm.

Finer WC grains increase hardness but reduce toughness, whereas coarser grains improve toughness at the expense of hardness. Co content also plays an important role in the hardness and toughness of cemented carbides. The higher the binder content, the more the material will tend to have the characteristics of metals, i.e. more ductile characteristics. Figure 2.5) summarizes the relationship between Co concentration, WC grain size, hardness, and fracture toughness. It can be seen that there are many grades available; therefore, depending on the application, it is important to achieve a good balance between hardness-wear resistance and fracture toughness. For example, in mining applications, the binder content varies between 6-15%Co and grain size above 1μm [14].

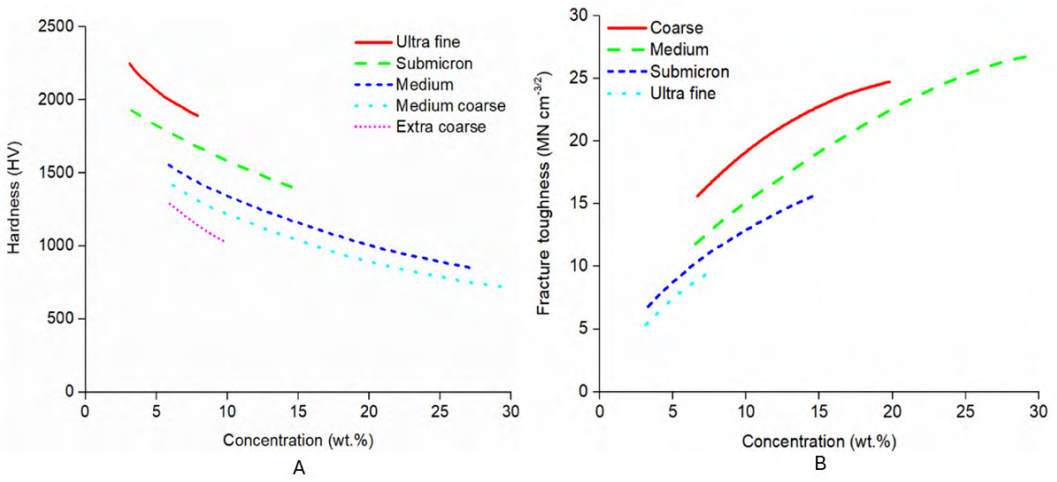

Figure 2.5: Mechanical properties of different WC-Co grades. A: Hardness vs %wtCo. B: Fracture toughness vs %wtCo. Adapted from [32].

2.2.1 WC: the hard phase

In W-C systems, three different carbides can exist: W_2C, WC and γ-WC_{1-x}. However, tungsten monocarbide, WC, is the major carbide in the W-C systems, and also the more relevant for cemented carbides [33]. WC has a simple hexagonal compact crystal structure (Figure 2.6 *A*), in which the lattice parameters are $a = 2.906$ Å and $c = 2.837$ Å [34]. WC is considered stoichiometric, although small amounts of additional elements such as Ta, Nb, or V have been found to dissolve in the carbide phase [35] [36].

During sintering an Ostwald ripening process occurs, meaning that smaller grains dissolve in favor of the growth of larger grains. The WC grain shape is illustrated in Figure 2.6 *B*, and it is mainly due to the asymmetry of C atoms within the crystal

structure. When the grains are faceted, the energy barrier for atom attachment on the surface is expected to be high. Thus, WC grain growth (nucleation of a new growth layer) is considered limited by interface reactions, compared to the spherical shape, where diffusion is the limiting factor [37]. Therefore, defects such as dislocations promote nucleation on a flat surface [38].

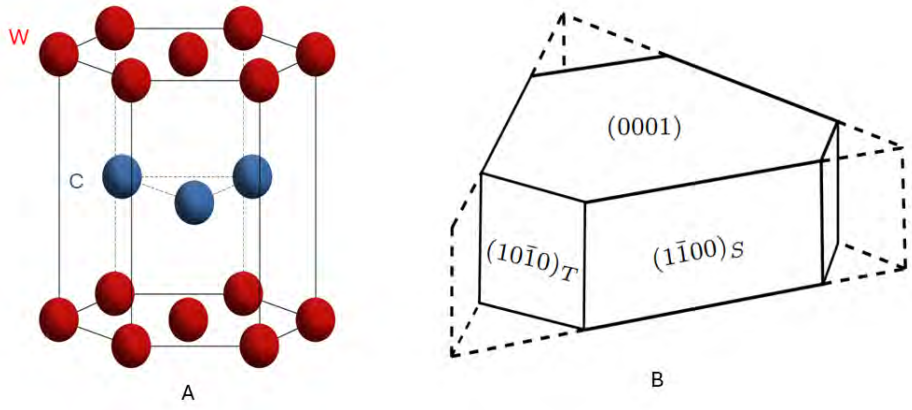

Figure 2.6: A: WC crystal structure. Adapted from [39]. B: WC crystal shape. Adapted from [40].

The shape and size of the WC grains are influenced by both C content and the type of binder used. For WC-Co cemented carbides, higher C content tends to produce more truncated grains and also promotes larger grain growth; alloys with lower carbon activity produce smaller and slightly rounder grains [41]. When iron-based binders are used, iron acts as a growth inhibitor, resulting in smaller grains compared to those in WC-Co systems. Conversely, WC-Ni systems exhibit enhanced grain growth, leading to a final WC grain size larger than that observed in WC-Co composites [42].

2.2.2 Co: the binder

Cobalt exists in two allotropic forms, a close-packed hexagonal cell, ϵ, and a face centered cubic one, α. Transformation from ϵ to α depends on the purity of the metal and on the increasing rate of temperature. Assuming the purest material and slow temperature changes, the transformation temperature is 421.5°C [4]. However, both phases coexist from room temperature up to higher temperatures. Cobalt is capable of dissolved large amounts of W and C at high temperatures, which stabilize the fcc phase at low temperatures. A fcc-hcp transformation can still occur, leading to hcp pools [41].
Another important property of cobalt is its magnetic behavior [43], which enables non-destructive testing methods for cemented carbides. These methods serve as quality control measures, particularly for evaluating grain size and carbon content [14].

2.2.3 Carbon influence and carbon window

In addition to Co content and WC grain size, carbon content also plays a crucial role in determining the properties of cemented carbides. When the composition corresponds to a W-C atomic ratio close to one, the phase WC and binder are stable. This is possible for only a narrow range of carbon concentrations. At lower carbon content, a brittle phase, called η phase, can precipitate. It can exist in two different forms, either $M_{12}C$ or M_6C, where M stands for metal and could be W, Co, Fe, or Ni [44]. Instead, when there is an abundance of carbon, graphite can be formed, either as flaked (when it is formed during solidification) or as nodular (when it is formed in the liquid binder) [4]. Neither η phase nor graphite is desired in the material, since they lower the mechanical properties.
During production, the material undergoes sintering, that is, heat treatment. It can be seen from Figure 2.7 that the carbon window varies with temperature. At 1000°C, the diffusion of solute atoms in the binder can be considered negligible, so it is common to assume the composition as frozen [45]. Consequently, there is a narrow window of carbon content that allows the so-called two-phase structure to be obtained upon sintering [24].

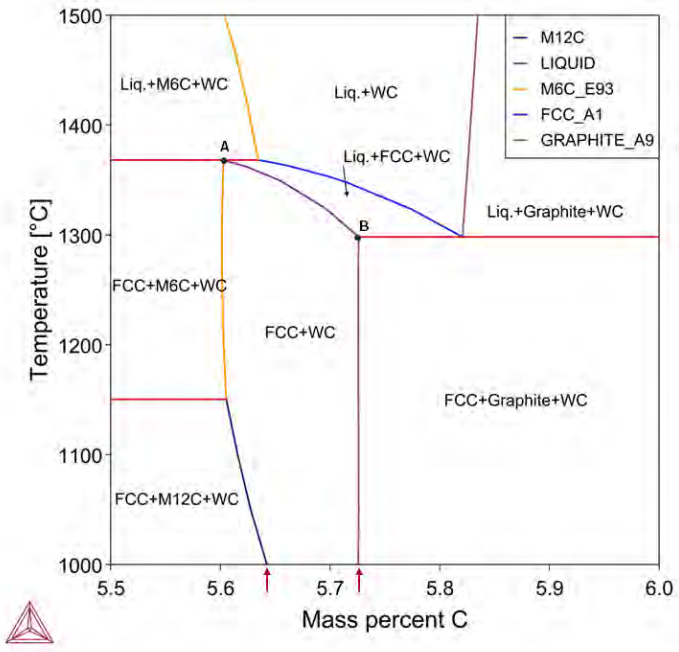

Figure 2.7: WC-Co isopleth [46].

2.2.4 Additives

To enhance the mechanical properties, microstructure and overall performance of WC–Co systems, various additives can be introduced. The addition of carbides such as TiC, TaC, VC and NbC leads to the formation of a secondary mixed cubic carbide phase (M,W)C, commonly called the γ-phase, where M represents Ti, Ta, or Nb

[14]. Among these, TiC stands out as a very hard and chemically stable carbide that contributes significantly to the wear resistance in WC-Co composites. It also functions as a grain growth inhibitor, although it is not the most effective for this purpose. In comparison, TaC and VC are the most widely used and are considered to be more efficient in controlling grain growth [42]. The addition of grain growth inhibitors can improve hardness, but this often comes at the expense of reduced toughness. Moreover, because of the complexity of these systems, predicting the final microstructure and properties remains a significant challenge. [47].

2.3 Alternative binders

Although WC-Co remains the most widely used combination in cemented carbides, interest in alternative metal binders has grown steadily since the 1980s. This shift is driven by several factors: Co is classified as a critical raw material due to its scarcity and ethical concerns related to extraction, as much of it originates from conflict regions [11]. Furthermore, Co faces increasing demand from other industries, particularly for lithium-ion batteries [48], and exhibits toxic and carcinogenic effects on human health [49]. Despite decades of research on alternative binders, comprehensive understanding of these systems remains limited. The greatest attention has been given to Fe and Ni, as their proximity to Co in the periodic table results in similar properties [50]. Both Fe and Ni are abundant and, compared to Co, cheap raw materials. However, altering the binder composition introduces significant challenges, as numerous factors influence the final properties. These include chemical interactions during sintering, such as wettability, shrinkage behavior, WC solubility in the liquid binder, and its effect on WC grain growth [51].
In this section, the principal alternatives to Co are presented.

2.3.1 Fe

Fe is a ferromagnetic metal which has a bcc crystal structure at room temperature, called α-Fe or *ferrite*. This structure allows a small concentration of carbon to enter in solution. At 912°C, a phase transition occurs from α-Fe to γ-Fe, also known as *austenite*, which has a fcc structure. The phase transition temperature depends on the carbon content. Austenite is non-magnetic and, because of the fcc structure, it can dissolve more carbon than bcc [52]. W and C stabilize the austenitic phase of Fe, which is the predominant structure in WC-Fe cemented carbides. However, Fe can dissolve lower amounts of W and higher quantity of C than Co. Fe is also acting as a WC grain growth inhibitor, compared to Co binders [42].
Fe binders can promote martensitic transformation, especially if other austenitic elements like Ni are present in the system. Having martensite in the structure can strongly influence the mechanical properties, in particular hardness, which is increased [53].
Using Fe as binder differs from Co in some aspects. From a thermodynamic point of

view, WC-Fe system has an extremely narrow C concentration required to achieve a two-phase structure (WC and Fe) at 1000°C [54]. The WC-Fe isopleth in Figure 2.8 is constructed with the same binder content as for the Co diagram in Figure 2.7. If the temperature interval between 1000-1500°C is considered the carbon window is non exciting. Furthermore, due to poorer wetting property than Co, Fe has impeded or delayed densification until the liquid state [51].

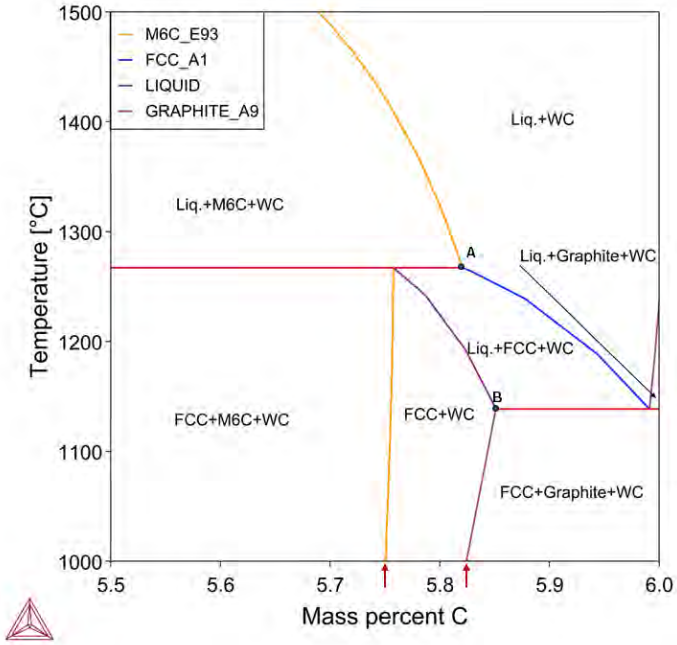

Figure 2.8: WC-Fe isopleth [46].

2.3.2 Ni

Pure Ni presents an fcc lattice, which is also kept when it is used as a binder in cemented carbides [55]. Ni is ferromagnetic, but it is less magnetic than Co and its magnetic properties are different, therefore quality control methods are not easy to use and interpret [55]. Ni has attracted significant interest as an alternative binder due to its excellent corrosion resistance and greater ductility compared to cobalt, which enhances wear resistance. However, WC-Co grades still exhibit superior hardness compared to WC-Ni [56]. Moreover, Ni tends to promote WC grain growth [42], making the addition of grain growth inhibitors a common practice in Ni-based systems.

Figure 2.9 illustrates the phase diagram isopleth for WC with a Ni-rich binder. Considering the same binder content as before (Figure 2.7), the carbon window is significantly wider than in the WC-Co and WC-Fe systems. This broader carbon window offers a considerable advantage, as it facilitates the formation of a two-phase structure.

In early studies, the WC-Ni system was typically assumed to exhibit a three-phase structure. This is because the two-phase region is significantly shifted toward lower

carbon content compared to the stoichiometric WC composition. As a result, WC-Ni samples prepared using stoichiometric WC often contained free carbon inclusions [57].
Ni-based binders show a higher liquidus temperature than the Co-based binders (temperature around 1433°C for Ni-based).

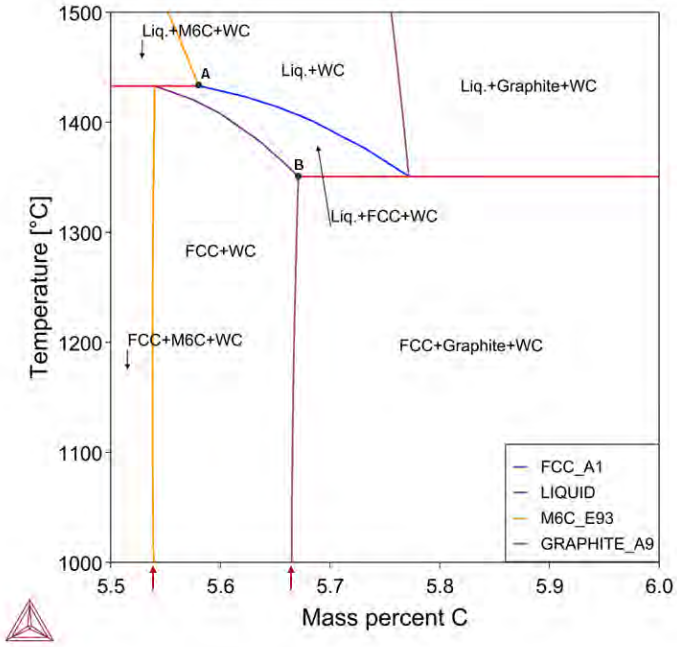

Figure 2.9: WC-Ni isopleth [46].

2.3.3 Fe-Ni-Co systems

Using binders composed solely of pure elements often results in mechanical properties inferior to those of the WC-Co system [54]. For instance, achieving a two-phase structure in Fe-W-C systems is challenging. To address this, mixed binder compositions have been studied, and Fe-Ni-Co alloys have been promising, combining good properties of the elements and also showing features not easily expressed by the elements on their own. The scientific literature reports a number of such systems, even though the overall knowledge is still too scarce to judge their applicability for industrial use [58].
When designing an Fe-rich based alternative binder, it is possible to tailor the binder phase crystal structure, ranging from austenitic (face-centered cubic, fcc) to martensitic (body-centered tetragonal, bct), or even a combination of both. Martensite provides higher hardness, whereas austenite offers greater toughness, allowing mechanical properties to be optimized through microstructural control. This design flexibility is achieved by controlling parameters such as the Fe/Ni/Co ratio, the C content, and the cooling rate after sintering [53][59].
Earlier studies have shown that Fe-rich binders containing martensite can achieve properties comparable to those of conventional WC-Co grades[58][60]. In particular,

WC-FeNi and WC-FeNiCo cemented carbides have been investigated. In general, the presence of Ni decreases the hardness, but increases the toughness, if compared to WC-Co grades. Depending on the specific binder composition, both hardness and toughness may be either superior or inferior to those of WC–Co grades. Wear tests have also been conducted, showing that alternative binders can provide improved wear resistance compared with WC–Co [58]. According to Liu [59] different composites exhibit excellent hardness to toughness combination, with 82Fe18Ni binder showing the best combination.
According to Gao's research [61], increasing the ratio between Fe and Ni results in enhanced wear resistance. Furthermore, the composition of the binder is also affecting the magnetic properties of cemented carbide: higher Fe/Ni ratio leads to higher coercivity and Co-magnetism.
As previously said, wear is influenced by the binder nature and in case of WC-Ni and WC-Fe a faster wear initiation and propagation have been observed compared to WC-Co [62].
Using two variable such as the binder amount and its composition, the number of possible combinations becomes enormous. Covering all of them would be impractical; therefore, this thesis focuses on the composition 50% Fe – 25% Ni – 25% Co. Generally speaking, one challenge is to have an acceptable carbon window, which allows to obtain a two phase structure without loosing the mechanical properties. Due to the narrowing of the carbon window, this option has not proven to be a successful alternative, and interest in it has fluctuated over time [63].
Figure 2.10 shows an example of a narrow carbon window for a 50% Fe – 25% Ni – 25% Co system; the span is from 5.705%wt to 5.755%wt, while the operational one is even narrower.
In this case, the eutectic temperature is 1293°C, so slightly higher than the pure Fe-based binder.

2.4 WC-50Fe-25Ni-25Co

Even though this system has been known since the 1980's [17], in the scientific literature there are not many researches related to it. The first insights into Fe–Ni–Co binder systems can be drawn from Uhrenius's work [54], who extensively investigated the phase equilibria and mechanical behavior of Fe–Ni–Co–WC cemented carbides. It was found that the addition of Co to Fe–Ni binders improves hardness and wear resistance, although the overall performance remains below that of conventional WC–Co alloys. Moreover, it was demonstrated that these binder systems are highly sensitive to C content: both graphite and η-phase precipitation occur readily outside a narrow carbon window. This intrinsic phase-stability limitation is particularly relevant for compositions with high Fe content, such as WC–50Fe–25Ni–25Co, where strict carbon control is required to avoid microstructural degradation.
According to Liu [59], this system represents the least favorable combination among the Fe-based binders examined in his study. It exhibited the lowest hardness and

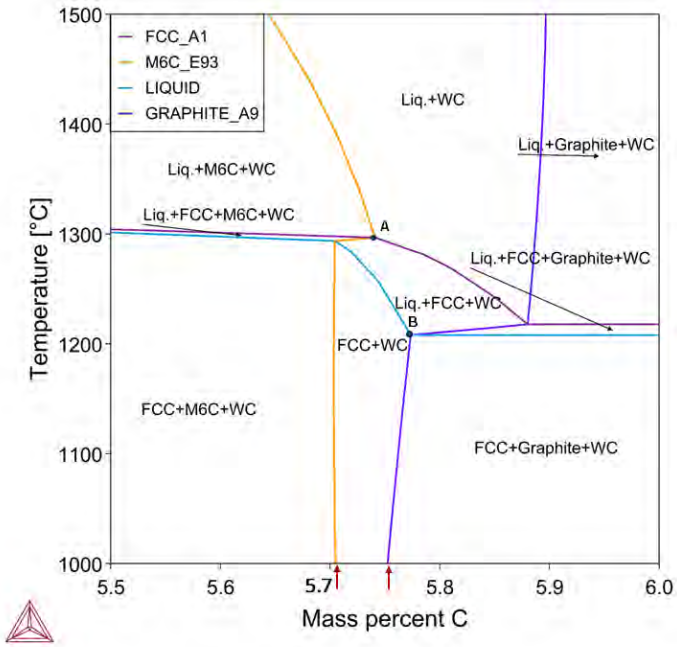

Figure 2.10: WC-Fe-Ni-Co isopleth [46].

fracture toughness, indicating that it is far from an ideal tool material. However, the binder content in Liu's work differs from that used in the present study, which may lead to variations in the results. Moreover, Liu states that only one sample for this composition was investigated, so any definitive conclusion cannot be draw.
Toller-Nordström investigated deformation-induced martensite formation in this composition using micro-scratching indentation. Electron backscatter diffraction (EBSD) revealed small martensitic grains within the binder phase [64].

Chapter 3

Methodology

In this chapter, the methods used during this work are presented.

3.1 Theoretical calculations and modeling

Thermodynamic modeling, based on equilibrium calculations, is a fundamental part of the CALPHAD (Calculations of PHAse Diagrams) methodology and is central to the ICME (Integrated Computational Materials Engineering) framework for advanced material design [65]. These computational approaches enable predictions of which phases are stable under varying temperatures and compositions, forming the basis for phase diagram construction, from which, for example, the carbon window for the material can be obtained.

3.2 Magnetic properties

The quality of cemented carbides is evaluated through non-destructive tests, such as magnetic property measurements, which make it possible to predict the final microstructure. Magnetic properties are feasible in traditional Co-based binders due to Co's ferromagnetic behavior. However, for cemented carbides with alternative binders, this method becomes less reliable, as very little work has been done coupling the magnetic properties and microstructure when other metallic elements are used as binder.

In a ferromagnetic material, the electrons structure forms coupling between the atoms that aligns in the so-called magnetic domains. These domains are locally magnetized and oriented in different directions. When a ferromagnetic material undergoes a magnetization–demagnetization process, the path followed during magnetization does not coincide with the path during demagnetization. This phenomenon is called hysteresis, and it occurs because the magnetic state of the material depends on its previous history. The hysteresis loop graphically represents the relationship between an applied magnetic field (H) and the material's magnetization (M). The condition at which increasing the magnetic field does not increase the magnetization of the material is termed as magnetic saturation (M_S), which corresponds to when

all magnetic domains have the same orientation. Magnetic saturation (M_S) is an important magnetic property for WC-Co cemented carbides [66]. It is demonstrated that there is a linear relationship between carbon content and magnetic saturation: when M_S increases, the amount of tungsten in solid solution in Co decreases (graphite precipitation) and vice-versa (η-phase formation) [14]. Equation 3.1 [65] shows the empirical relation:

$$M_{\mathrm{S}} = m_{c_o} \left(M_{\mathrm{S}}^{c_o} - k m_W^{c_o} \right) \tag{3.1}$$

where m_{Co} is the mass percentage of Co, M_S^{Co} is the magnetic saturation of pure Co, m_W^{Co} is the mass percentage of W in the binder and k is a fitting parameter.
The amount of W in the binder is dependent on the overall C content. By measuring M_S, therefore, becomes an indirect method to evaluate the C balance in the material. For WC-Co cemented carbides, it is however common to use the Co-magnetism, usually referred to as Co-m%, instead of the M_S. Co-m% is the percentage of magnetization of the sample relative to the theoretical magnetization of pure Co at the same mass.
It is however not yet known whether this linear relationship is still valid when referring to alternative binders.
Coercivity is the strength of the reverse magnetic field required to reduce the magnetization of the material to zero [67]. It reflects how strongly the magnetic domains are pinned and how difficult it is to reverse their orientation. In cemented carbides, this pinning effect is influenced by the WC–Co microstructure: the cobalt binder contains magnetic domains, and their movement is hindered by the WC–Co interfaces. Fine-grained carbides have more interfaces, which increase domain pinning and therefore require a higher coercive force to demagnetize. Conversely, coarse-grained carbides have fewer interfaces, allowing domains to move and rotate more freely, resulting in lower coercivity. The relation between coercivity and WC grain size is reported in Equation 3.2 [68]:

$$H_C = 1.44 + 0.04 m_{CO} + \frac{12.47 - 0.37 m_{CO}}{d_{WC}} \tag{3.2}$$

where m_{Co} is the mass percentage of Co and d_{WC} is the average grain size of WC.
Coercivity is measured using instruments such as coercive meters or coercive magnetometers, which extrapolate the value from the hysteresis curve [68].
Figure 3.1 summarizes the relationship between magnetic properties and microstructure.

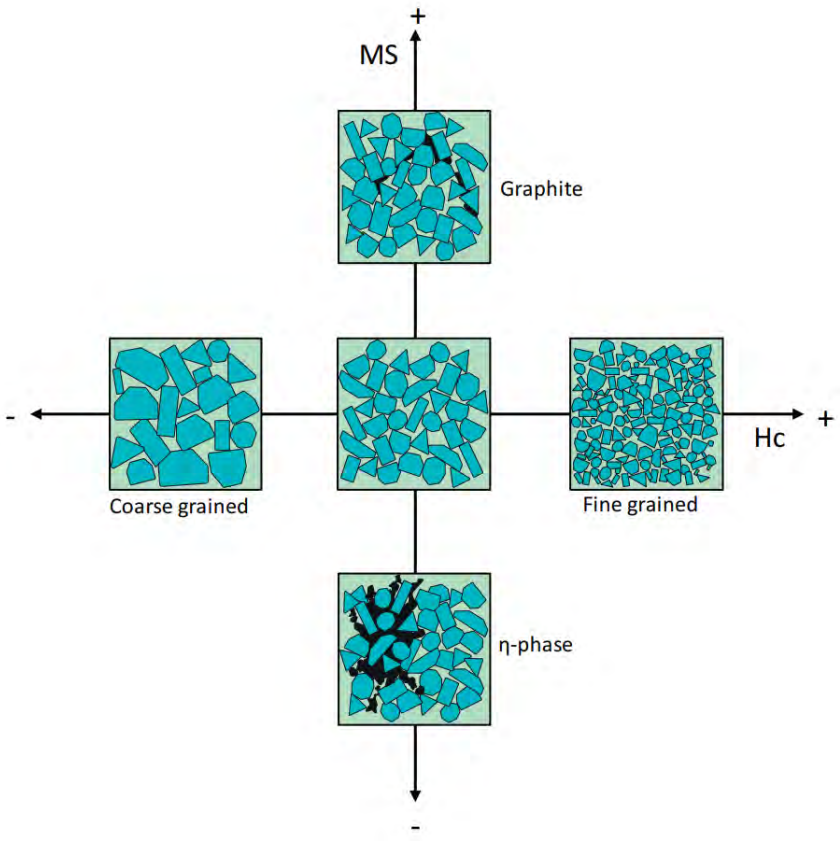

Figure 3.1: Relationship between coercivity (Hc), magnetic saturation (M_S) and the microstructure of cemented carbides. Image from [14].

3.3 Density

Density is determined following Archimede's principle according to the Equation 3.3:

$$\rho = \frac{m_1 \rho_w}{m_1 - m_2} \tag{3.3}$$

where ρ is the density of the sample, ρ_w is the density of distilled water, m_1 is the mass of the sample in air and m_2 is the mass of the sample in distilled water.

3.4 Chemical analysis

Elemental analysis was performed using X-ray fluorescence (XRF), a powerful technique that identifies the elements present in the sample and quantifies their concentrations. Carbon content was determined separately through combustion analysis using a LECO instrument.

3.5 Light Optical Microscopy

Light Optical Microscopy (LOM) is a powerful tool for observing the overall microstructure of cemented carbides, for instance porosity and additional phases, as

η-phase and graphite. LOM uses visible light that is reflected or transmitted through one or more lenses. What appears is a magnified image of the sample surface. Despite its great importance and usage, LOM has a magnification limit of around x1000. Usually, when cemented carbide samples are observed, sample surface is etched, to evidence some of the microstructural features, such as the different phases. The most common etchant for cemented carbides is the so-called Murakami's solution, which is prepared by adding potassium ferricyanide ($K_3[Fe(CN)_6]$), potassium hydroxide (KOH) and water (H_2O). The exact formulation and application time may vary, depending not only on the material but also on which phase is wanted to be examined. Using LOM, one can easily observe the structure affected by the etching. For example, the etchant kept for a small time, e.g. five seconds, highlights the η-phase, which appears yellow (Figure 3.2(a)). Graphite, on the contrary, is not affected by the Murakami's solution (Figure 3.2(b)). Therefore, this is a quick method to determine whether the material is in the desired carbon window.

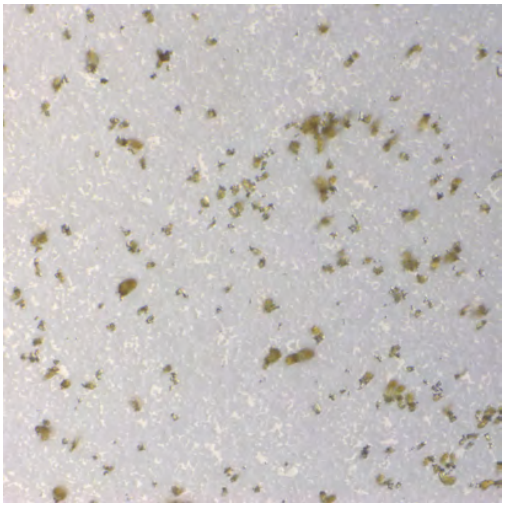

((a)) η-phase (yellow) immersed into the carbide structure

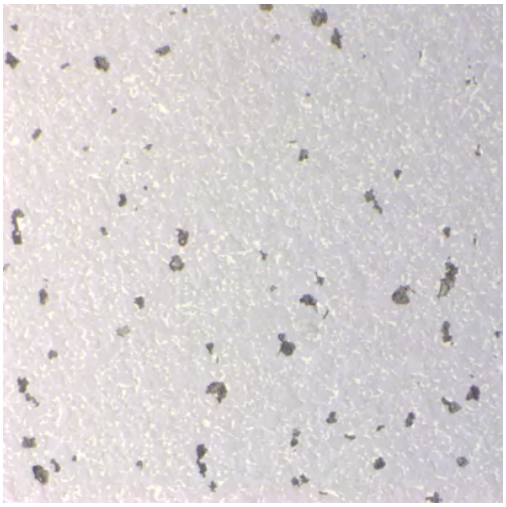

((b)) Nodular graphite (black) immersed into the carbide structure

Figure 3.2: LOM micrographs

3.6 Stereo Microscope

A stereo microscope is a type of optical microscope designed for low-magnification observation, typically ranging from x3 to x80. It uses reflected light from the specimen's surface and, thanks to the slightly different viewing angles of its paired objectives, produces a three-dimensional image of the sample.

3.7 Scanning Electron Microscope

The scanning electron microscope (SEM) is an instrument that uses a focused electron beam that creates magnified images with magnification higher than that of the LOM

[69]. In SEM, an electron beam is focused on the sample placed under vacuum. The interaction between the sample and the electron beam is represented in Figure 3.3.

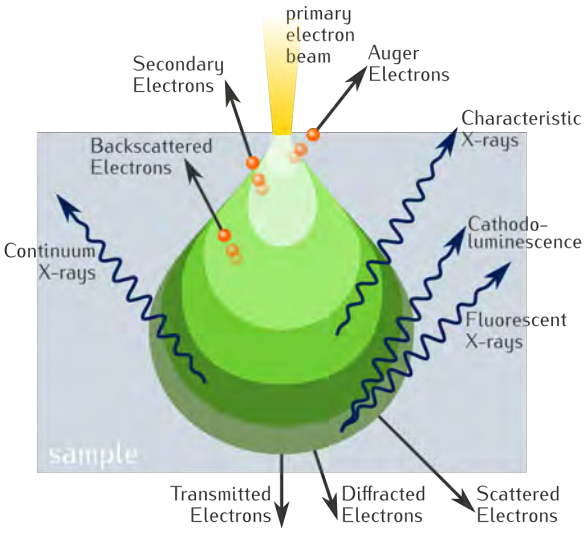

Figure 3.3: Interaction volume [70].

This volume extends from the surface to several micrometers deep, depending on factors such as acceleration voltage (i.e., beam energy) and sample composition [71]. In general, the higher the voltage, the higher the interaction volume. Moreover, the interaction volume is larger when the sample is lighter, and vice-versa. With different detectors attached to the SEM microscope, different signals coming from the interaction volume can be collected and analyzed, providing not only an image of the sample surface, but also chemical and crystallographic information.

3.7.1 Secondary electrons and back-scattered electrons imaging

The electron beam, commonly referred to as the primary electron (PE) beam, interacts with the atoms in the sample primarily in two ways (Figure 3.4). When a PE ejects an electron from the surface of the sample, an electron, known as a secondary electron (SE), is emitted and it has a very low energy if compared to the PE one (0-50 eV vs 10-50 keV). When a PE undergoes elastic scattering with the atoms in the sample, it produces a backscattered electron (BSE), which energy is comparable with the PE one. As shown by the interaction volume in Figure 3.3, secondary electrons are emitted by the first atomic layers, so the resulting image has a topographic character. The number of BS electrons strongly depends on the atomic weight of the atoms, thus heavier atoms generate more BSE compared to lighter ones.
Image analysis can be performed using SEM images acquired with a backscattered electron (BSE) detector, allowing for quantification of the area fraction of the phases.

3.7.2 Energy Dispersive Spectroscopy

When a secondary electron (SE) is ejected from an atom, an electron from the outer shell can transition to fill the vacancy, releasing excess energy in the form

of X-rays. Each element emits X-rays with characteristic energies, which can be detected and used for chemical analysis in an SEM. This technique, known as Energy Dispersive Spectroscopy (EDS), is a powerful tool commonly employed for rapid chemical characterization of samples.
In the case of cemented carbides, EDS analysis is a good analysis method to analyze metallic elements. However, the technique is limited for the light elements and here C cannot be quantified due to several reasons. First, it is a light element, so its characteristic X-rays have very low energy and EDS detector cannot accurately detect them with high precision. Indeed, those are easily absorbed by the detector window or the sample surface, and they often overlap with signals from other elements. Second, sample surfaces often exhibit carbon contamination from the environment or during preparation. Third, surrounding heavy atoms, such as W, can absorb carbon's characteristic X-rays, preventing them from escaping the sample.

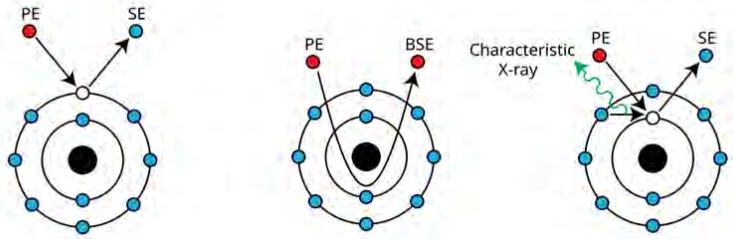

Figure 3.4: The emission mechanisms for SE, BSE and X-rays. [70]

3.7.3 Electron Back-Scattered Diffraction

Electron Back-Scattered Diffraction (EBSD) is a technique used to study the crystallographic structure of materials. The sample is placed in the SEM chamber and tilted at an angle of 70 degrees to the beam (Figure 3.5), to have a high number of diffracted electrons. The incident electrons interact with the sample and then are scattered in many directions, losing a small part of their initial energy. Some of these scattered electrons collide with the crystal lattice planes, satisfying Bragg's diffraction law: $n\lambda = 2d\sin\theta$, where n is an integer number, λ is the wavelength of the electrons, d is the spacing of the lattice planes and θ is the angle of incidence. These diffracted electrons, hitting the phosphorus detector, form a pair of curved lines (called "Kikuchi bands") for each of the lattice planes. The diffraction pattern is created by the overlapping of multiple Kikuchi bands, which thus depend on the crystal lattice and its orientation [72].
From an EBSD post-processing several information can be extracted, such as the grains orientation, the grain size, the distribution of phases. Information about dislocations in the material, elastic properties, and phase transformation event can be extracted [73] [74].

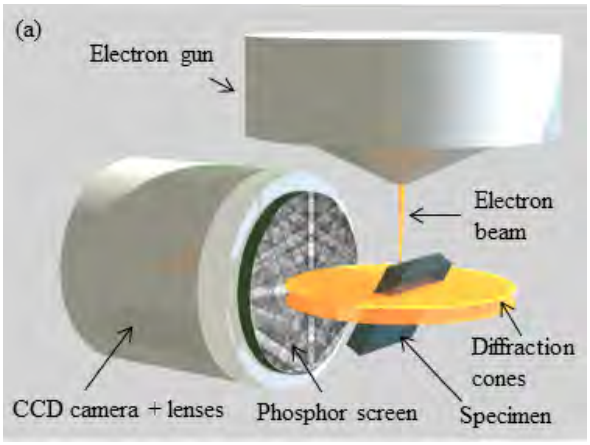

Figure 3.5: The EBSD hardware setup inside an SEM. [75]

3.8 Mechanical characterization

The materials were tested with different techniques to obtain their mechanical properties.

3.8.1 Hardness

Hardness is the ability to resist plastic deformation and for cemented carbides it can vary depending on the binder composition, its content and distribution, and on the size of WC grains. Hardness is evaluated by running the Vickers Hardness Test, in which a square-based pyramid (with an angle of 136°) diamond indenter is pressed into the surface of the test piece using a prescribed force for a certain time. When the force is removed, the length of the indentation diagonals is measured. According to the ISO 6507-1 standard, the Vickers hardness values are calculated following Equation 3.4 [76].

$$HV = 0.102 \times \frac{2F \sin\left(\frac{\alpha}{2}\right)}{d^2} \tag{3.4}$$

where: F is the applied force (in N)

α is the angle between opposite faces of the diamond (136°)

d is the average indentation diagonal length (in mm)

3.8.2 Fracture toughness and Palmqvist method

Fracture toughness is the material property that quantifies its ability to resist crack propagation. When referring to crack propagation and fracture mechanics, different modes of crack propagation exist (e.g., opening, in-plane shear, out-of-plane shear). The crack propagates in the material only when the stress intensity factor is greater than a critical value, K_c. The fracture toughness value is usually referenced when the crack propagates under plane strain conditions. In this case, it is known as the plane strain fracture toughness K_{Ic}.

K_{Ic} is obtained from tests on specimens with an appropriate geometry for plane strain conditions and containing a defined crack geometry. Since there is no standard method for hardmetals, the Palmqvist method is usually used instead.
The Palmqvist method relies on the measurement of the length of the cracks at the corners of a Vickers indentation (HV30)(Figure 3.6) and through calculations the Palmqvist toughness W_K is obtained [77].

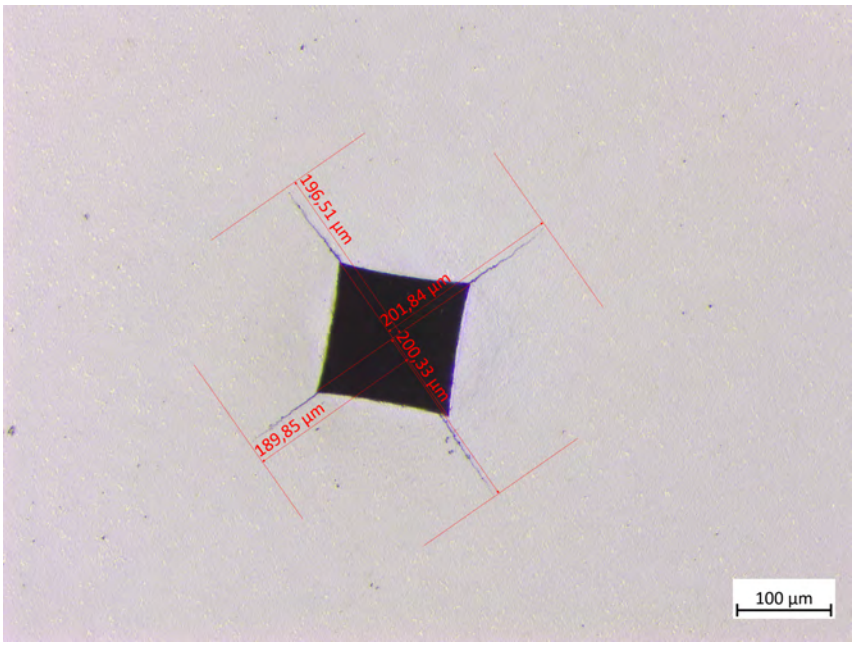

Figure 3.6: Cracks length measurement through LOM picture

Equation 3.5 is used to calculate W_K, which corresponds to K_{Ic} for cemented carbides. The unit is MN $m^{-3/2}$.

$$W_K = A\sqrt{H}\sqrt{\frac{P}{T}} \tag{3.5}$$

where: A is an empirical constant with value of 0.0028
H is the hardness in N mm^{-2}
P is the indent load (in N)
T is the total crack length (in mm)

Even if the Palmqvist method overestimates toughness, a good correlation is claimed between K_{Ic} and W_K for WC-Co systems [78].

3.8.3 Wear test

A Sandvik internal rock turning wear test is run to imitate the wear seen on the top of the insert during top hammer rock drilling. Figure 3.7 shows a schematic of the test setup. A sample is mounted to an arm which pushes it against the granite with a set force, while also moving along the lateral direction to let the bit face new rock

each revolution. The granite rock is cylindrical and it is mounted in a lathe, thus it can rotate at a constant speed. The sample is weighted before and after the test, and the mass loss is converted to volume loss [79].

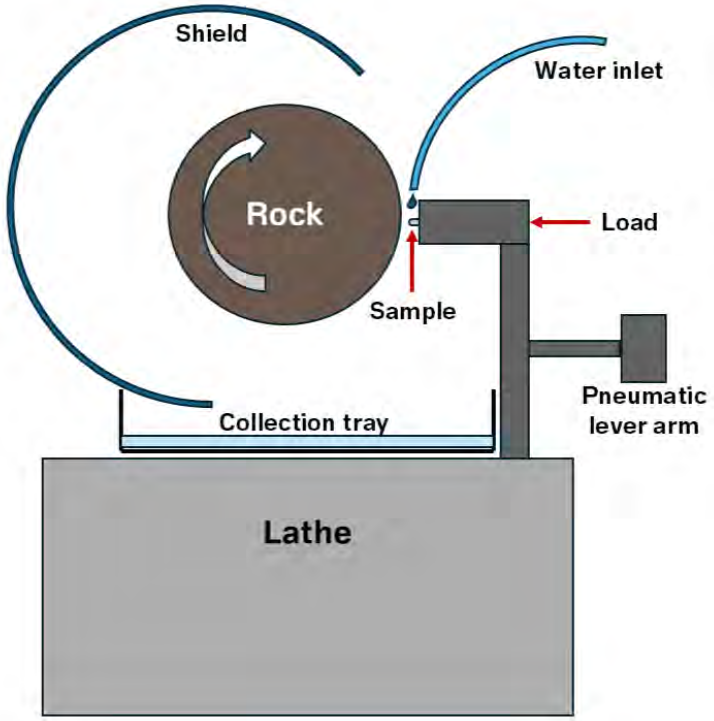

Figure 3.7: Cross section of the schematic setup for the rock turning wear test. The sample moves from the long axis of the rock cylinder. Adapted from [79].

3.8.4 Crush test

Crush test is essentially a compression test, where the sample is subjected to a compressive load until failure. The sample is placed on a plate and another plate is put in contact with the tip of the insert sample. At this point, the load is applied and the software records load vs. displacement until failure. From this test key properties as load at break, fracture energy and extension at break can be evaluated.

Chapter 4

Experimental details

To address the research questions, the following experimental approach was adopted. A series of materials with varying C contents was produced to map the two-phase window of the selected composition. The goal was to obtain materials spanning from the three-phase structure WC–binder–η to the three-phase structure WC–binder–graphite.
All materials were characterized in terms of structure and selected properties, while mechanical properties and detailed microstructural analyses were performed only for the materials that resulted in a two-phase structure.
The experimental procedures followed in this work are presented in this chapter.

4.1 Calculations

All the phase diagrams shown in this work were calculated using ThermoCalc software and the TCFE13 database [46]. The binder composition is based on Prakash's work [17], where the binder composition is a mixture of 50 wt% Fe, 25 wt% Ni, and 25 wt% Co. Further, the total binder content is tailored for mining grade composition. Taking these parameters into account, the phase diagram or isopleth of this material was calculated and the result is shown in Figure 4.1.
It can be noticed that the theoretical equilibrium C-window is very narrow, indicating that it could be difficult to obtain a two-phase structure upon sintering. However, as very little work has been done on these material systems one objective of this thesis is to map the system and compare it with the calculations.
The phase diagram for this system can be compared with the pure WC-Co, WC-Fe and WC-Ni systems. For such comparison, based on the binder composition, the exact number of moles for each binder element was calculated at the η-phase limit. The total sum of these moles represents the binder's molar content in the system, which is necessary to construct WC-single-element binder phase diagrams that are directly comparable.

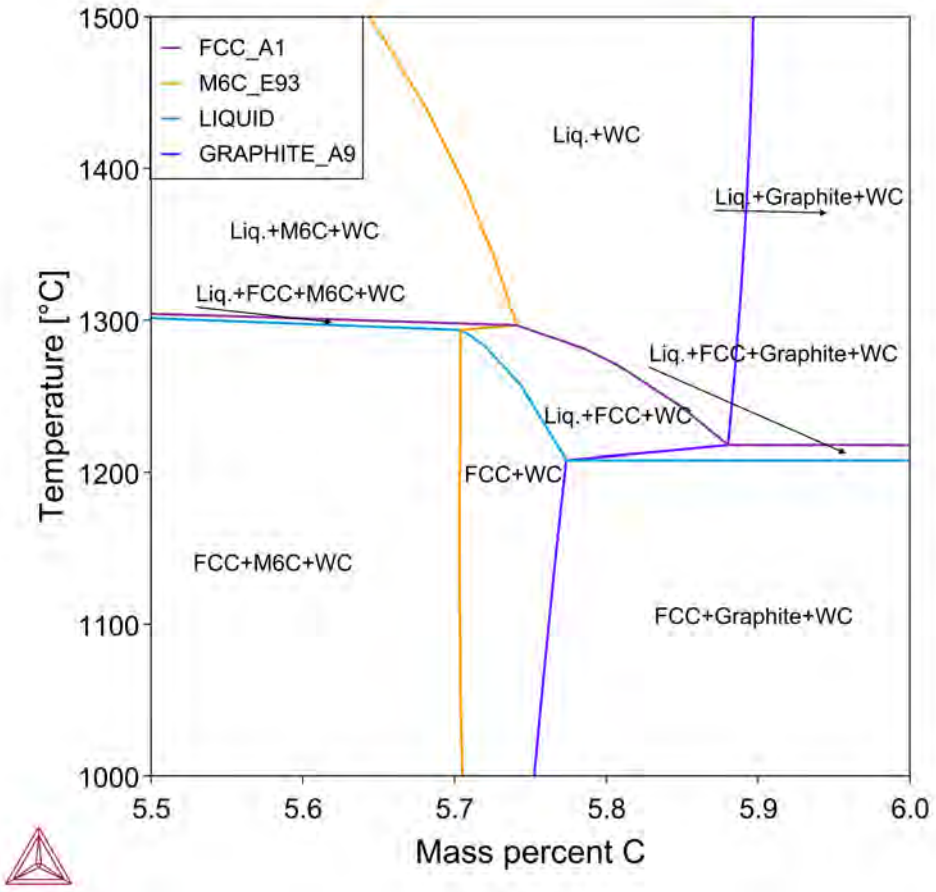

Figure 4.1: Phase diagram of the selected material, calculated with ThermoCalc and the TCFE13 database [46].

4.2 Materials

In this study, to map the C window, eight materials were designed with a constant Fe/Ni/Co ratio, while varying the total C content to cover the transition from the η-phase field to the graphite field. Additionally, each material was sintered using two different sintering cycles, at two different temperatures to evaluate the influence of sintering temperature on the final microstructure. The prepared materials are listed in Table 4.1; material 1 corresponds to the lowest C content, and increasing numbers indicate progressively higher C levels.
Selected samples were sent for the chemical analysis to measure the metallic elements and C content.

4.3 Samples manufacturing

4.3.1 Milling and Drying

All materials were produced in small lab scale ball mills. In addition to the powder raw materials, cemented carbide milling bodies, milling liquid (ethanol), and a pressing agent (polyethylene glycol, PEG) was added to the mills. The milling time

Table 4.1: Samples series

Sample Name	C content
01	1
09	2
02	3
10	4
03	5
04	6
05	7
06	8

was set at 8 h for all the batches. After milling the powders were pan dried.
For the material composition ending up within the two-phase structure based on the structure from 1500°C sintering, new mills were produced to obtain more powder. These were repetitions of the previous one, so it is assumed to have the same composition.

4.3.2 Pressing and Sintering

All materials were pressed in a test sample geometry called SNUN, which is a shape of a small cube, used for structural and basic properties characterization, For the materials showing a two phase structure, an additional pressing to an insert geometry GT7S100A was performed for mechanical properties testing.
Sintering was carried out at two different temperatures: 1410°C and 1500°C. The sintering cycle performed was similar to the one shown in Figure 2.2. A code was used to differentiate the samples from the two sintering, 02 for the 1410°C sintering and 03 for the 1500°C sintering. For example, the sample with C content 2 sintered at 1410°C is called 09_02.

4.3.3 Post treatment

For one of the two-phase samples pressed as an insert, a Sandvik internal post-treatment was applied in order to study the effect of this process. Different process parameters were used and will be referred to P1, P2 and P5 in the following description.

4.4 Sample preparation

In this section, details on the sample preparation are presented.
The samples were cut in half using ATM QCUT 250 cutting tool. The samples were cut at half of their width to obtain a cross-section precisely through the center, ensuring that the measured properties accurately represent the bulk material. Thereafter, one half is embedded in a conductive resin (bakelite), using ATM OPAL 460 equipment. It is essential to use conductive resin, as it ensures proper operation of the SEM by preventing charging effects on the sample surface.
The last step is to grind and then polish the surface. The aim is to have the so called "mirror-like" surface. This was done in four steps using the ATM SAPHIR 550 grinding and polishing machine. Between each step, it is crucial to thoroughly clean the samples to avoid cross-contamination from larger particles. Each polishing stage employs a specific lubricant suspension. These suspensions consist of monocrystalline diamond particles with a size of 9, 3 and 1 μm. After each step, the samples are first cleaned manually, then placed in a beaker containing ethanol or acetone and subjected to ultrasonic cleaning.
The samples prepared for EBSD analysis required ion beam polishing, with the specific preparation details provided Table 4.2. The equipment used is Hitachi IM4000 system. Ion beam polishing is needed to obtain a flat and defect-free surface

Table 4.2: Ion beam polishing steps.

	Acceleration Voltage	**Time**	**Angle**
Step 1	6 kV	90 min	∼4°
Step 2	2 kV	20 min	∼4°

that is required for good indexing in the Electron Backscattered Diffraction technique (see Paragraph 4.6.3). Furthermore, through ion beam polishing the scratches from the mechanical one can be removed, allowing better imaging in the SEM. Figure 4.2 shows how the ion beam hits the sample surface. The sample is mounted on the holder and secured with carbon tape. After insertion into the chamber, it is tilted to a specified angle, denoted as θ. Once the chamber reaches the required vacuum level, the ion beam is activated and the sample is set to rotate. All the samples prepared for EBSD by ion beam polishing have used a tilting angle of 4°.

4.5 Properties measurements

4.5.1 Hc, Com% and density

The magnetic properties, Hc, Co-m%, were measured using a dedicated holder; each sample was first placed in the coercive magnetometer and then in the magnetic saturation tester, from which the corresponding values were obtained via their

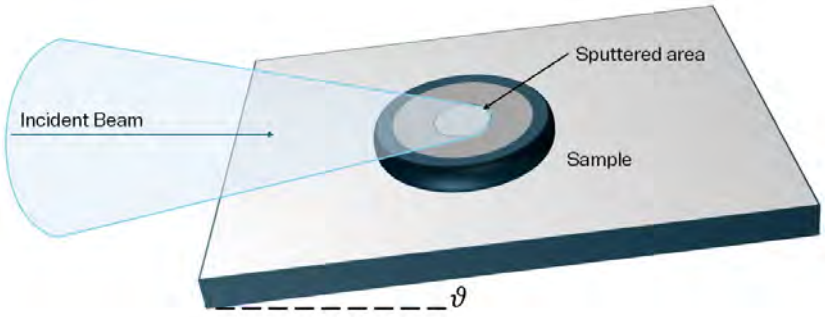

Figure 4.2: Ion beam polishing scheme. θ represents the angle.

software. Finally, density was determined by recording the sample's weight and volume using a hydrostatic balance, with the software calculating the final density value.

4.5.2 Hardness and Toughness

In this study, HV20 hardness tests were performed, where '20' denotes a load of 20 kgf applied for ten seconds. To ensure statistical reliability, five separate indents were made and evaluated for each sample, and the average value was then calculated. To get first indications of the toughness, Palmqvist toughness was evaluated from HV30 indents ('30' stands for the applied load of 30 kgf). It is known that this method shows a good relation for WC-Co systems and will here be used to show trend in toughness also for this system. However, the absolute values cannot be determined.
The length of the cracks produced by the indents is measured using LOM. Through specific software, indents' cracks were measured. This measure is needed for the calculation of toughness, according to Palmqvist method (see Paragraph 3.8.2). Also, in this case, for each sample five indents were made, and the average value was calculated to ensure statistical significance.
To evaluate the effect of post-treatment, HV3 mapping was performed. For hardness mapping, sample 02_02_i was selected to test different post-treatment processes, as shown in Table 4.3.The "i" stands for the samples pressed with the insert shape.

Table 4.3: Post-treatment programs associated with sample 02_02_i.

Sample	Program
	P1
02_02_i	P2
	P5

Multiple series of indents were applied to each sample. Indents along the same line were spaced 0.1 mm apart. The first line was positioned 0.3 mm from the cross-section edge, followed by subsequent lines at distances of 0.6, 1.2, 2.4, and 4.8 mm from the

edge. In this case, the applied load was 3 kgf.

4.5.3 Wear and Crush

The wear test was conducted using an internally re-build turning lathe, called stone lathe. The stone lathe wear test employed Red Bohus granite at a theoretical rotational speed of 196 rpm. The target load was 10 kg, with a target distance of 300 mm and a feed speed of 0.9 mm/s.
For each composition within the two-phase structure, two samples having the insert shape were tested. Every sample is weighted before and after the test, so that the measured mass loss can be converted into volume loss per turning distance. The stereo microscope was used to observe and photograph the tips of the samples after the wear test.. The software also allows measurement of the tip area and diameter. ZEISS SteREO Discovery.V12 microscope was used.
For the crush test two samples were tested for each composition within the two-phase structure, using an Instron machine. The samples were pre-loaded with 300 N; after pre-loading, the test was started and the samples compressed until failure. The instrument measures load vs displacement, therefore properties as load at break, fracture energy and extension at break can be calculated. In this study, only fracture energy is evaluated.

4.6 Microscopy for structure characterization

Microscopy is essential for the evaluation of the microstructure of cemented carbides, as their performance is strongly governed by features such as grain size, binder distribution, and the presence of other phases. In this study, a combination of optical and electron-based techniques were used to investigate those characteristics: LOM, stereo microscope, SEM, EDS, and EBSD.

4.6.1 Structure evaluation and overview imaging

During this work, the LOM used to investigate the microstructure was ZEISS AX10 microscope. Overview pictures of the samples were collected to investigate the structure of the samples, whether they are in the two- or three-phase structure. To do so, each sample was etched on half of its surface with Murakami's solution (see Paragraph 3.5) for five seconds.
Overview micrographs were acquired using a Jeol JSM-7800F scanning electron microscope equipped with a backscattered electron detector. Six images were captured for this purpose and used to quantify the binder phase. The obtained area fraction of the binder phase is assumed to be comparable with the volume fraction owing to stereological principles [80]. The settings used are reported in Table 4.4.

4.6.2 Image Analysis

4.6.2.1 Binder phase quantification

Since WC appears lighter than the binder phase due to atomic weight reasons (see Paragraph 3.7.1), this feature can be used to separate the phases during image analysis of SEM images. The software used for this purpose is ImageJ [81], which allows to set a threshold on the gray level to distinguish WC (the grey phase in Figure 4.3(a)) from the binder, which will appear as red as shown in Figure 4.3(b). The output of the software is the percentage of the analyzed area that is below the set threshold, and this value is then used as the percentage of the binder in the picture, i.e. the binder area fraction.

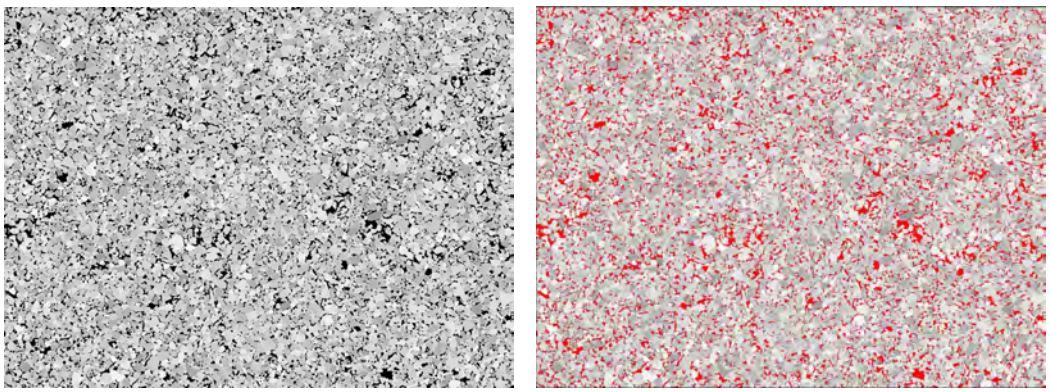

((a)) Initial SEM image **((b))** Binder phase in red

Figure 4.3: Image analysis.

4.6.2.2 Binder phase grain size

Using ImageJ it is also possible to determine the binder true grain size from EBSD orientation maps (explained in Paragraph 4.6.3). In particular, two different methods were used: the Linear Intercept Method (LIM) and the thresholding method described in Paragraph 4.6.2.1. For the LIM, different straight lines are drawn in different directions on the image. Then the number of times these lines intersect the grain boundaries is counted and if the intercept passes through a triple point it counts for 1.5 . Equation 4.1 explains how the grain size G is calculated.

$$G = \frac{L}{N} \tag{4.1}$$

L is the total length of the test line and N is the number of intercepts counted.
The length and number of lines should be sufficient to obtain a statistically valid count. The average G is then calculated.
In the case of the thresholding method, the output from the software is the total number of grains counted and their average area. Assuming these are circular, it is then easy to calculate the mean diameter, i.e. the grain size. To increase the reliability of the result, the grains were also manually counted from the image.

4.6.3 Detailed structure analysis for the two-phase materials

EDS X-ray maps were acquired using SEM equipped with an Oxford Ultim Max Infinity 100 detector. Two maps were taken at two different magnifications. Detailed parameters are summarized in Table 4.4. These maps allowed evaluation of the sample's composition within the mapped area. The sum of the elements of the binder is then used for comparison with the binder evaluation made with the other techniques.

Table 4.4: BSE and EDS settings details. WD is the Working Distance.

	Magnification	**Acceleration Voltage**	**WD**
BSE	x900	15 kV	10 mm
EDS	x900, x200	15 kV	10 mm

EBSD was performed to evaluate microstructural features that cannot be resolved by standard SEM imaging. EBSD allows to characterize the crystallographic structures, the grain orientation and distribution.
EBSD analysis was performed in a Jeol JSM-7800F scanning electron microscope equipped with an Oxford instrument Symmetry S3 EBSD detector. The operational settings are reported in Table 4.5. All six samples (3 from 1410°C sintering, 3 from 1500°C sintering) showing the two phase structure were analyzed. For each sample, maps at two magnification using two different step sizes were analyzed, to both have a detailed analysis and to be able to cover and calculate the real grain size for the binder phase. The analysis raw data were post-processed using a Sandvik internal routine within the MATLAB [82] and MTEX [83] software, which gave different output: grain orientation, phase fractions and phase statistics.

Table 4.5: Instrument, analysis, and post-processing settings

	Magnification	
Instrument settings	**x200**	**x900**
Acceleration voltage [kV]	20	20
Working distance [mm]	∼15	∼15
Probe current settings	12	12
Analysis settings		
Step size [μm]	0.5	0.1
Map area [μm^2]	590x440	130x98
Post-processing settings		
Critical misorientation angle [°]	3	3
Definition of smallest grain [pixels]	4	4

Chapter 5

Results and Discussion

5.1 Structure overview and basic properties

Table 5.1 reports the observed structure for all samples having the SNUN geometry. In general, the C window was mapped, observing all the expected structures, from WC-binder-η to WC-binder-graphite (see Appendix B, Figure B.1). It can be pointed out that two different graphite morphologies have been observed. The important result is that three composition showed a two-phase structure. Thi shows that the C balance can vary 0.06 wt% and still obtain a two-phase structure, while the theoretical production window is predicted to be narrower, i.e. 0.03 wt%. Compared to the Co system, this span is 0.084 wt%.

Table 5.1: Observed structure for the SNUN samples.

	Observed structure	
Carbon level	**1410°C**	**1500°C**
1	η-phase	η-phase
2	η-phase	two-phase
3	two-phase	two-phase
4	two-phase	two-phase
5	two-phase	graphite(flaked)
6	graphite(flaked)	graphite(flaked)
7	graphite(nodular)	graphite(nodular)
8	graphite(nodular)	graphite(nodular)

The sintering temperature affects the resulting microstructure, as shown in Table 5.1. In particular, for the 1410°C sintering, the transition between the η-phase and the two-phase region shifts toward a higher C content compared to the 1500°C sintering. Table 5.2 shows the Co-m% values a the sintering control sample added for this purpose. It can be seen that for the 1500°C sintering, Co-m% is higher than for the

1410°C, meaning that the furnace atmosphere has been richer in C, affecting the phase stability in the samples. Hence, the two phase region is then shifted to lower C content in the samples sintered in the 1500°C.

Table 5.2: Control samples: density, coercivity, and magnetic saturation.

Control	**Sintering**	**Density** $[g/cm^3]$	**Hc** $[kA/m]$	**Co-m** [%]
REF_02	1410°C	13.1585	11.95	8.748
REF_03	1500°C	13.1129	10.5	9.085

If this is a direct effect of the temperature difference or just variations between different sintering charges need to be further investigated. In coming comparisons this difference will result in a shift in C level for the two-phase sample between the different sinterings. However, this shift will be neglected and the cause of it needs deeper analysis. Hence, following a comparison between the samples will be done focusing on whether a temperature effect can be seen on structure and properties, i.e. comparing trends for the sample series sintered at different temperatures.
Figure 5.1 illustrates how sample densities change with C content and the applied sintering temperature. Density can indicate the presence of η-phase, graphite, or pores: the latter two reduce density, whereas the former increases it. Porosity was observed on most of the samples through the LOM. It can be easily seen that at higher C content, when graphite precipitates, the density quickly drops to lower values. In case of 1500°C sintering, the highest density is reached in the two-phase structure, while 1410°C it is reached for a sample having η-phase. In general, the shape of the two curves is comparable. Moreover, density is rather constant inside the two-phase region.

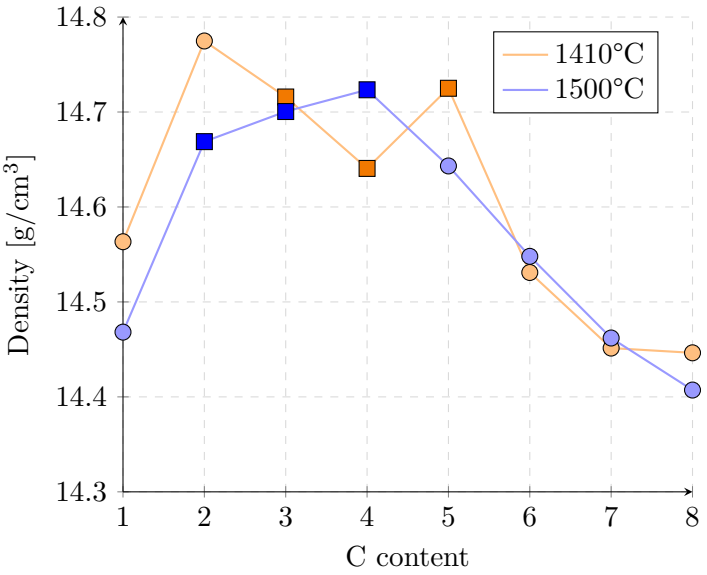

Figure 5.1: Density vs C content. The squares highlight the samples having the two-phase structure.

Figure 5.2 illustrates the variation of coercivity (Hc) with C content for the two series with different sintering temperatures. The squares highlight the samples having the two-phase structure. Both curves exhibit a similar trend, characterized by an initial increase to a peak followed by a decrease. This peak occurs at the same C content for both sinterings, but in case of 1410°C sintering it is the first sample having the two-phase structure, while for 1500°C sintering it is the second one.

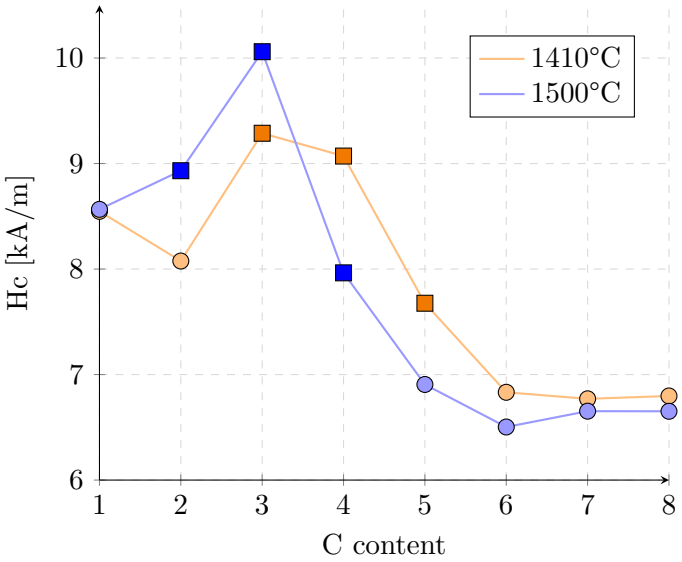

Figure 5.2: Hc vs C content. The squares highlight the samples having the two-phase structure.

When measuring the second magnetic property, both values for magnetic saturation (Ms) and Co-m% were recorded. Since these properties change with C content in the same way (see Appendix B, Figure B.2) it is chosen to present the results for Co-m%. Figure 5.3 depicts the variation of Co-m% with C content for the two sintering temperatures. The overall trend is comparable: the curves show an increase in Co-m% with an increasing C content, comparing between the lowest and highest one. Inside the two-phase region, the differences between the values are small. For both sinterings, however, there is a slight increase in Com% to a peak, occurring in the second samples having the two-phase structure, followed by a decrease, and finally another increase. In particular, for both the curves, the first peak is centered on the second sample having two-phase structure.

For Co-based cemented carbides, there is a linear relationship between Co-m and the carbon content. This observation is also made by Linder [68] in his research, even though in that case the alternative binder is Ni-based instead of Fe-based. Since the differences within the two-phase samples are so small in this study, it is very hard to verify this relationship.

The graph in Figure 5.4 represents how hardness varies with C content. It can be seen that the trend is the same for the two sintering temperatures. When graphite forms, hardness begins to decrease, and the greater the amount of graphite, the lower the hardness becomes, as expected. η-phase effects also hardness, but not as much as

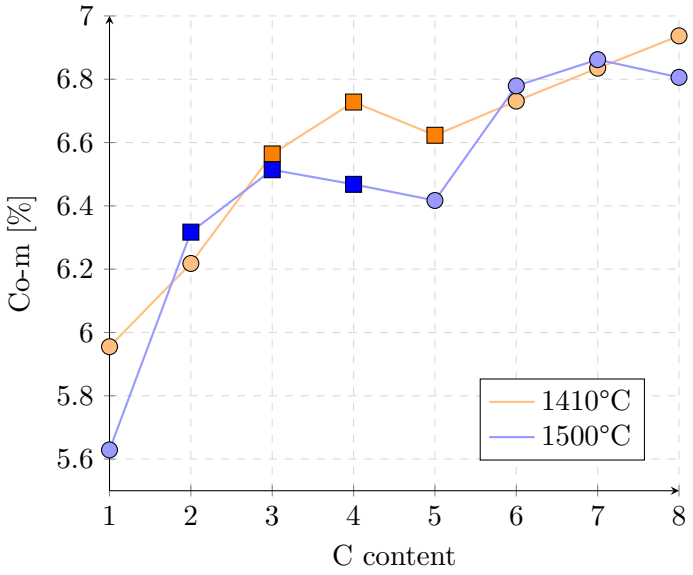

Figure 5.3: Com% vs C content. The squares highlight the samples having the two-phase structure.

graphite does. The higher values of hardness are reached in the two-phase structure. Inside the two-phase region, the values of hardness of the samples are comparable. Considering that the usual measurement error is ±30 Vickers, it can be seen that all the samples having the two-phase structure show the same hardness value. No difference in trend or values can be seen when the two temperatures are compared.

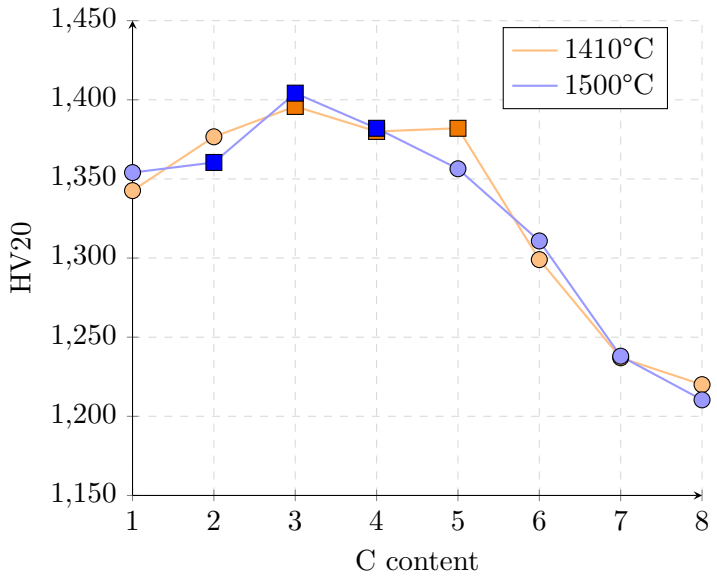

Figure 5.4: HV20 vs C content. The squares highlight the samples having the two-phase structure. Further details presented in Table A.1 in Appendix A.

The graph in Figure 5.5 represents how fracture toughness, evaluated using Palmqvist method, varies with C content. Relative values are used here to compare the samples, calculated by normalizing each value to the lowest one.
It can be seen that the trend differs between the two sintering temperatures: the

1500°C samples results much more tough, compared to the 1410°C samples. In case of the 1500°C samples, toughness increases until a peak, with a following lowering; for 1410°C samples, there is not a peak, and toughness increases with increasing C content.
It is possible that when the graphite content is low formed during solidification as flakes, which might deflect cracks during propagation. Conversely, at higher graphite contents, the phase becomes more continuous (nodular) and weaker, allowing cracks to pass through it rather than being deviated. This behavior could explain why this phenomenon is not observed in 1410°C samples, here the peak and subsequent decrease are absent.
Focusing only on samples having the two-phase structure, fracture toughness steeply increases with increasing C content. This is observed for both sinterings.
The values measured through the Palmqvist method cannot be fully accurate for different reasons. It is an optimized method for cemented carbides with Co-based binders and not alternative binders. As the binder composition is changed, the constant A in Equation 3.5 might not be valid. Further, one source of error is that the measurement of the crack length is made by an operator using the LOM, so it open to human error. Nevertheless, these results show that the toughness changes with increasing carbon content within the two-phase structure, indicating a clear trend.

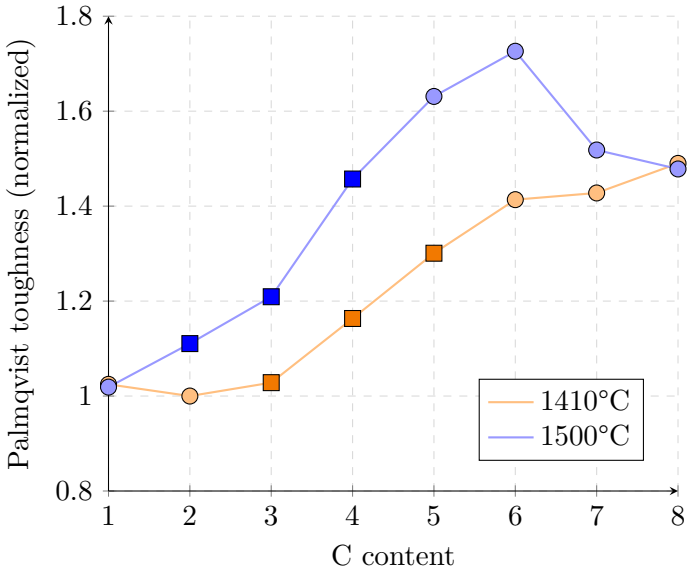

Figure 5.5: Palmqvist toughness (normalized) vs C content. The squares highlight the samples having the two-phase structure. Further details presented in Table A.2 in Appendix A.

Figure 5.6 illustrates the relationship between hardness and fracture toughness. It is evident that the presence of graphite reduces the hardness of the material, making it softer. In contrast, the η-phase does not significantly lower hardness but results in a material that is extremely brittle.

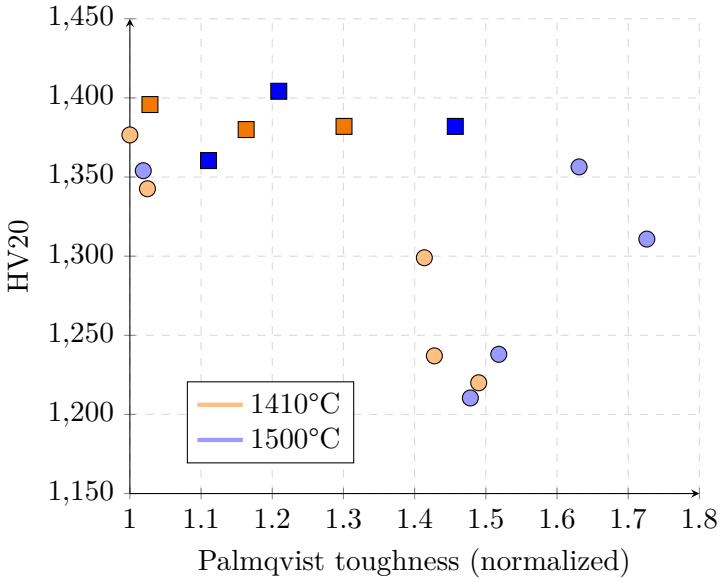

Figure 5.6: HV20 vs Palmqvist toughness (normalized). The squares highlight the samples having the two-phase structure.

5.2 Chemical Analysis

The results from the chemical analysis (LECO and XRF) are presented in Figure 5.7 and Figure 5.8. The analyzed samples include those sintered at 1410°C: specifically, three with a two-phase structure, one exhibiting the η-phase, and one containing graphite. Figure 5.7 shows the measured C content% for the different C levels. It can be seen that the trend is linear, except for one value. This deviation may be related to several things, for instance inhomogeneities within the sample analyzed. In any case, the result is consistent with what is expected from mill prodution, as the samples designed with progressively higher C levels indeed show an increasing C content.

It is though interesting to note that the trend in the two-phase structure is the same as the one observed for the Co-m%.

Figure 5.8 shows the analyzed content of the binder elements. The amount of Fe and Ni follows the nominal one, while Co does not. This can be explained due contamination from the WC-Co milling bodies used in the milling process. The metallic elements in the binder were during material design kept constant for all samples, and the analysis values confirm this.

Focusing on Co, it appears to be shifted from the expected value by a constant factor, independent of composition. This factor, calculated in Table **??** (Appendix A), can be approximated to 1.1. This observation is important because it indicates that all samples are affected in the same way by the process or that there are error in the XRF method used. This needs to be further investigated.

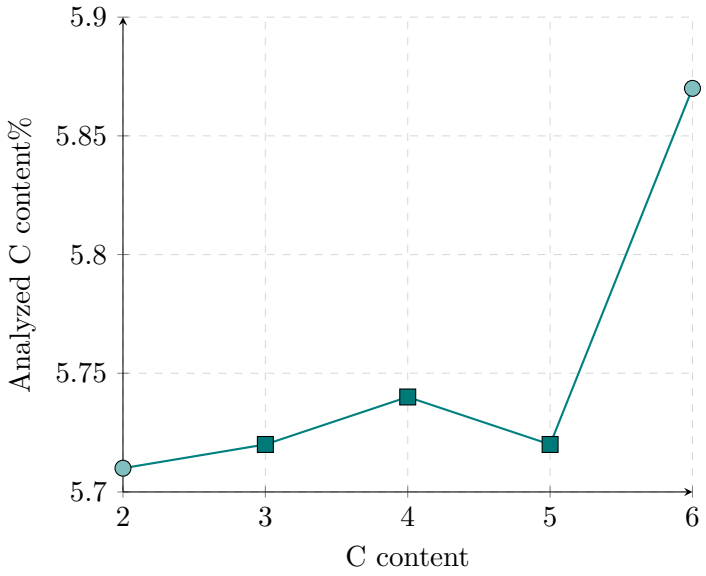

Figure 5.7: Analyzed C content for the different C levels. The square highlights the samples having the two-phase structure.

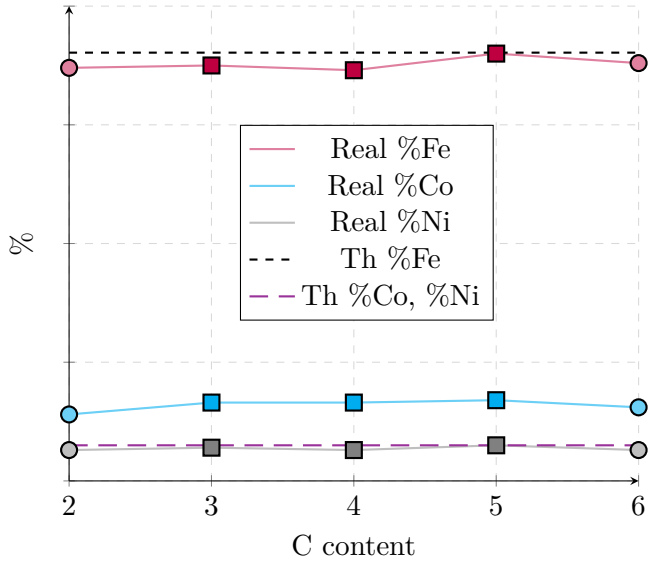

Figure 5.8: Analyzed (Real) metallic binder elements composition using XRF and nominal (Th) composition vs C content.

5.3 Detailed structure analysis using EDS and EBSD

It is of interest to compare the structure of the two-phase samples from both the sinterings. Specifically, chemical composition, phase fraction and statistics.
For the chemical analysis using EDS, the analysis was run twice: the first time while observing the samples using the BSE mode, the second time while running EBSD analysis. The main difference is in how the sample is placed in the chamber. For the former, the sample is not tilted, whereas for the latter it is, which will affect the interaction volume. In both cases, the C percentage was excluded in the software because C is difficult to quantify with EDS.

5.3.1 Phase fraction

In Table 5.3 normalized phase fractions can be seen from post-treated data for different samples and different sinterings, acquired through EBSD with x900 magnification.

Table 5.3: Normalized phase fraction for 1410°C and 1500°C samples.
Normalization against the sample with the lowest C content for each sintering.

	1410°			**1500°C**		
Sample	**02_02**	**10_02**	**03_02**	**09_03**	**02_03**	**10_03**
WC%	Bal.	Bal.	Bal.	Bal.	Bal.	Bal.
Tot binder%	**1.00**	1.17	1.16	**1.00**	0.74	0.97
Iron FCC %	**1.00**	1.17	1.16	**1.00**	0.72	1.00
Iron BCC %	**1.00**	4.00	1.00	**1.00**	0.75	0.25
BCC/Tot binder	**1.00**	3.41	0.86	**1.00**	1.01	0.26

The binder phase is reported to consist primarily of austenite (FCC), indicating that within the two-phase structure window, its structure remains unchanged. It can be seen that the Iron BCC (martensite) fraction is very small and probably this value depends on misindexing during EBSD analysis.
Evaluation of the binder phase area fraction from EDS and EBSD can be compared with those obtained from the binder phase evaluation using ImageJ, as reported in Table 5.4. All data compared is from analysis/images at magnification x900. No clear trend can be identified. It is important to note that the ImageJ analysis may be influenced by human error, meaning that the reported values might not be highly precise. For the image analysis the noted trend is that the binder fraction is larger for all samples sintered at 1500°C compared to those sintered at 1410°C.
The values from both the EDS anayses can be considered constant, but to obtain more statistics re-measurement are suggested.
EBSD seems to result in lower binder fractions compared with the EDS, this is

obvious if EBSD data are compared with EDS tilted, since this analysis is on the exact same area.

Table 5.4: Normalized comparison of ImageJ, EBSD and EDS (both flat and tilted) binder phase fraction (%) for 1410°C and 1500°C samples.

	Sample	ImageJ	EBSD	EDS (flat)	EDS (tilted)
GPS1410	**02_02**	1.06	1	1.32	1.32
	10_02	0.83	1	1.06	1.20
	03_02	0.89	1	1.06	1.16
TAV1500	**09_03**	1.40	1	1.08	1.11
	02_03	1.67	1	1.44	1.47
	10_03	1.30	1	1.13	1.10

Note: ImageJ and EBSD will evaluate an area fraction, while EDS evaluate sum of metallic elements in wt%.

5.3.2 WC grain size and distribution

EBSD analysis provides valuable insights, particularly regarding WC grain size and distribution. From the EBSD analysis, the area of each WC grain is measured and converted into an equivalent circle diameter, assuming the WC grain shape to a sphere. Overall, the results (Figure 5.9, Figure 5.10 and Table 5.5) show equal sizes for all two-phase samples independent of C content and temperature.

Figure 5.9 presents the WC relative-area grain size distributions for both sintering temperatures. The curves are nearly overlapping, indicating that the C content has little to no effect on the WC grain size distribution. For the 1410°C sintering (Figure 5.9 left), the lowest C content (blue curve) results in a slightly narrower distribution for the larger grains. However, if D_width is considered, it can be seen that for increasing C content, it does not change. As the C content increases, the distribution shifts marginally toward larger grain sizes. However, these differences are minimal, can be considered negligible, and likely fall within the analysis error. This trend does not occur for the 1500°C sintering samples shown in Figure 5.9 (right), where the lower C content (red curve) does not correspond to the smaller grains. Taking into account that the scaling on the x-axis is different for the two graphs, it can be seen that in case of 1500°C sintering the distribution approaches nearly 5 μm, while for 1410°C sintering the curve ends around 4 μm, meaning that the 1500°C sintering samples have a larger tail in their distribution.

To better understand the large grains within the WC grain size distribution, it is helpful to examine the logarithmic representation shown in Figure 5.10, where the y-axis indicates the logarithm of the number of grains with a given diameter (Sandvik internally called Nordgren distribution). Compared to relative area distributions, the logarithmic representation provides a clearer view of what occurs at the extremes of

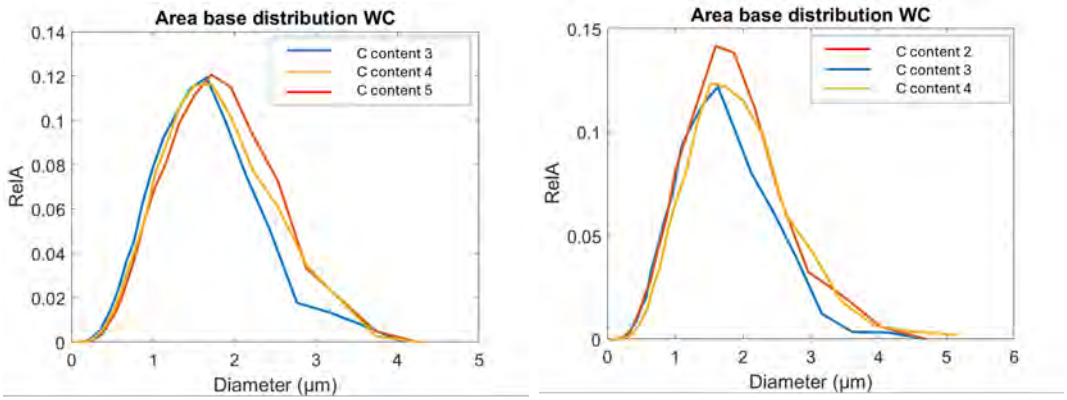

Figure 5.9: WC relative area based grain size distribution for 1410°C (left) and 1500°C (right) sintering. Colors follow increasing carbon content: blue, yellow, red for 1410°C; red, blue, yellow for 1500°C.

the distribution. In this study, it is particularly useful for highlighting the coarse-grain tail.

For 1410°C samples, the blue curve, corresponding to the lowest C content, shows a higher number of small grains (< 1 μm), placing it above the other curves in this range. For larger grains, the blue curve falls below the others, with a noticeable divergence starting around 2.5 μm. Conversely, the red curve, representing the highest C content, exhibits the opposite trend: it is lower for small grains and higher for large grains. The yellow curve, corresponding to intermediate C content, lies between the two extremes. These results are consistent with previous observations; However, this shows a slight indication that the C content may influence the distribution, but this effect is negligible.

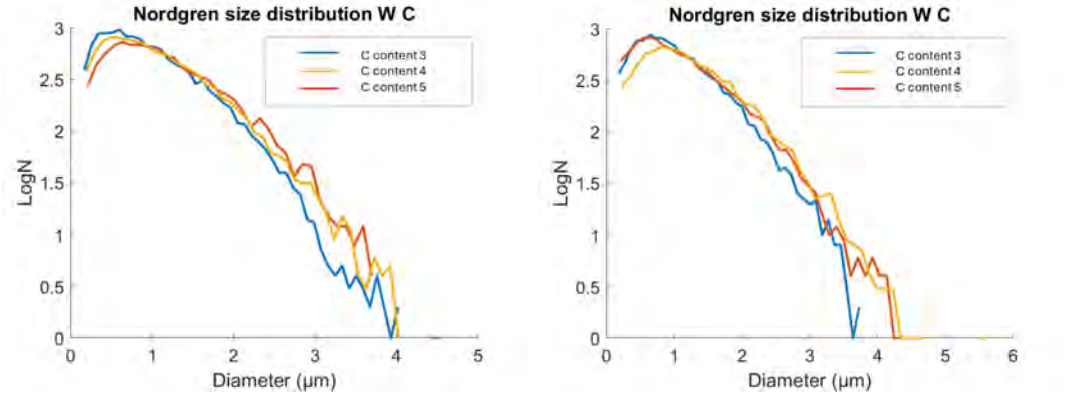

Figure 5.10: WC Nordgren size distribution for 1410°C (left) and 1500°C (right) sintering. Colors follow increasing C content: blue, yellow, red for 1410°C; red, blue, yellow for 1500°C.

For 1500°C sintered samples, the trend does not strictly follow C content, as previously noted. The red curve, representing the lowest C content, lies between the other two.

The blue curve shows the highest number of small grains and the lowest number of large grains, despite having a higher C content. The main difference between the red and blue curves become noticeable from about 2 μm onward; before that, they are almost overlapping. The yellow curve, corresponding to the highest C content, displays the smallest number of fine grains and the largest number of coarse grains. Table 5.5 presents the statistics of WC grain diameters. It is shown that higher sintering temperature results in slightly larger grains, which confirms the trend observed in Figure 5.9.

Table 5.5: WC grain size statistic values for 1410°C abd 1500°C samples..

	1410°			**1500°**		
Sample	**02_02**	**10_02**	**03_02**	**09_03**	**02_03**	**10_03**
D05 (μm)	0.6	0.7	0.7	0.7	0.7	0.8
D10 (μm)	0.8	0.8	0.9	0.9	0.8	0.9
D50 (μm)	1.5	1.7	1.7	1.8	1.6	1.8
D90 (μm)	2.5	2.8	2.8	2.9	2.7	3.0
D95 (μm)	2.9	3.1	3.1	3.3	3.0	3.4
D100 (μm)	4.3	4.5	4.5	5.1	5.0	5.5
D_width	1.1	1.2	1.1	1.2	1.2	1.1
N of grains	11981	10078	8989	9440	10869	8009

D05, D10, D50, D90, D95, and D100 represent particle size percentiles, indicating the size below which 5%, 10%, 50%, 90%, 95% and 100% of the particles or grains in the sample fall. For example, D50 corresponds to the area weighted average grain size, and is the equivalent circle diameter corresponding to when the combined areas of the WC grains are 50% of the total area for all WC grains [84]. The D50 values remain nearly constant across all samples, confirming that WC grain size does not depend on C content. Furthermore, D50 is nearly constant regardless the sintering temperature; the differences appear in the upper range of diameters, where D90, D95, and D100 show noticeably larger values. Another important aspect is the width of the grain size distribution, referred to as D_width. This parameter indicates how far D10 is from D90 relative to the midpoint D50, as expressed in Equation 5.1:

$$D_width = \frac{D90 - D10}{D50} \tag{5.1}$$

The D_width value is nearly identical across all samples, confirming once again that the primary differences between them are linked to the presence of larger grains (above D90), which occur at higher C content and higher sintering temperatures. However, the statistic for the larger grains is poorer than for the smaller ones.
The cumulative area fraction curves, from which the data were extrapolated, are

provided in Appendix B (Figure B.3).

Figure 5.11 compares EBSD maps colored based on equivalent circle diameter (ECD) of each grain across all samples. The 1410°C samples are shown on the left, and the 1500°C samples on the right, with C content increasing from top to bottom.

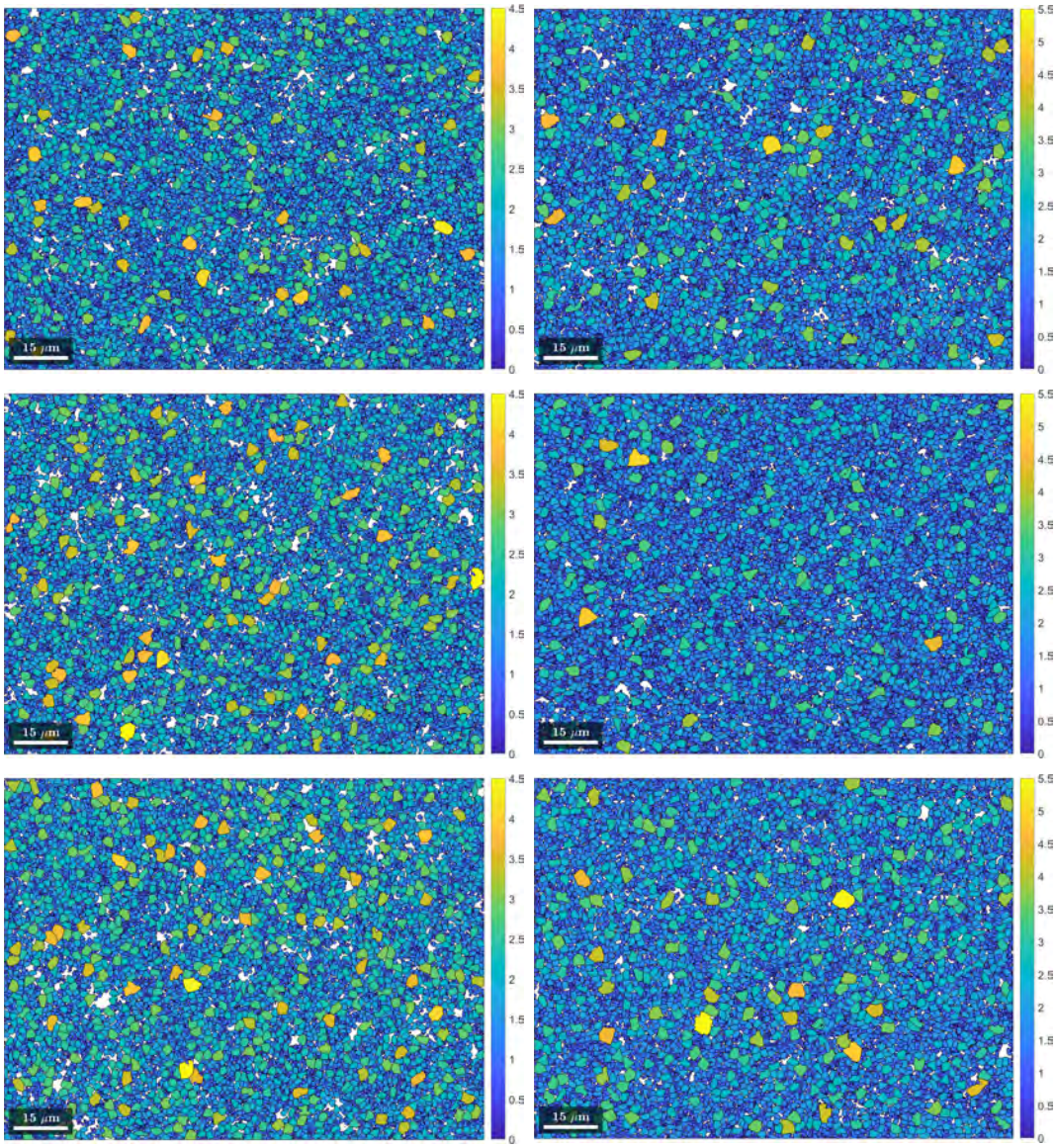

Figure 5.11: EBSD maps colored based on ECD. Comparison between WC grain size. Left: 1410°C samples; 02_02 (top), 10_02 (center), 03_02 (bottom). Right: 1500°C samples; 09_03 (top), 02_03 (center), 10_03 (bottom)

The findings of this study are consistent with those reported by Roulon [85] for cemented carbides containing a pure Fe binder. In that investigation, the effect of carbon content on WC grain growth was systematically evaluated, and it was demonstrated that carbon content does not influence the resulting WC grain size. The results presented here also align with those of Liu [59], who demonstrated that the presence of Fe in the binder suppresses WC grain growth. However, this is not in agreement with what has been seen regarding the Co systems. It is known from the CO-based cemented carbides that higher C content should result in larger, more

truncated WC grains, while lower C content should produce smaller and rounder grains [41]. Further, the results found in this study do not agree with what was found by Danielsson [86] studying cemented carbides with a pure Ni binder. It was seen that the C content had a large effect on WC grain size and distribution.

5.3.3 True binder grain size evaluation

This section presents an evaluation of the binder phase, focusing on its grain size and the number of grains. Binder grains are significantly larger than the WC grains (binder grains >50 μm vs WC grains <10 μm), meaning that a single binder grain typically surrounds multiple WC grains. This should not be confused with the size of binder phase pockets, which only indicate the presence of binder material between WC grains and do not represent the actual binder grain size. The calculated results based on image analysis of EBSD orientation maps at low magnification (x200) are summarized in Table 5.6. Here results from both hand count and count from the ImageJ software are presented. The size is evaluated using both ECD (Equivalent Circle Diameter) and LIM (Linear Intercpets Method) methods.

Table 5.6: Comparison of ImageJ count, Hand count, ECD (Equivalent Circle Diameter), and LIM (Linear Intercepts Method) for 1410°C and 1500°C samples. ECD and LIM are expressed in [μm].

	Sample	ImageJ count	Hand count	ECD	LIM
1410°C	**02_02**	48±6	37±8	82.05±5.57	80.59±10.80
	10_02	45±6	39±4	85.26±5.37	78.03±7.42
	03_02	65±18	62±21	70.78±9.93	59.87±5.49
1500°C	**09_03**	25	25	112.59	117.42
	02_03	39	38	90.25	72.53
	10_03	52	52	77.74	56.26

In case of 1410°C samples, two different EBSD maps for each composition were taken and analyzed, and the values reported in the table are averages of the measurements, with the corresponding standard deviation included. Two different techniques were employed to evaluate grain count and grain size, and both produced consistent trends across the samples, which is an encouraging outcome. While neither method is highly precise due to potential human error, the agreement in trends strengthens the reliability of the results, even if the statistics are poor. The data indicates that true binder grain size is influenced by both C content and the sintering temperature: higher carbon C corresponds to smaller binder grains, whereas higher sintering temperatures lead to larger grains. Although the differences are not substantial, they are likely affected by statistical limitations due to the small samples number.
Figure 5.12 presents the images used for the evaluation. These were generated by a Sandvik's internal MATLAB script based on EBSD analysis data. The trend highlighted in the table is also visually evident: the grains in the right column, corresponding to the higher sintering temperature, appear larger and therefore fewer in number. Each color in the image corresponds to a specific grain orientation, i.e. specific grains. In Appendix B (Figure B.4) the maps from the second measurement on the 1410°C samples can be found. Also in that case the same trend is shown, with

visually notable the decreasing of the binder grain size.

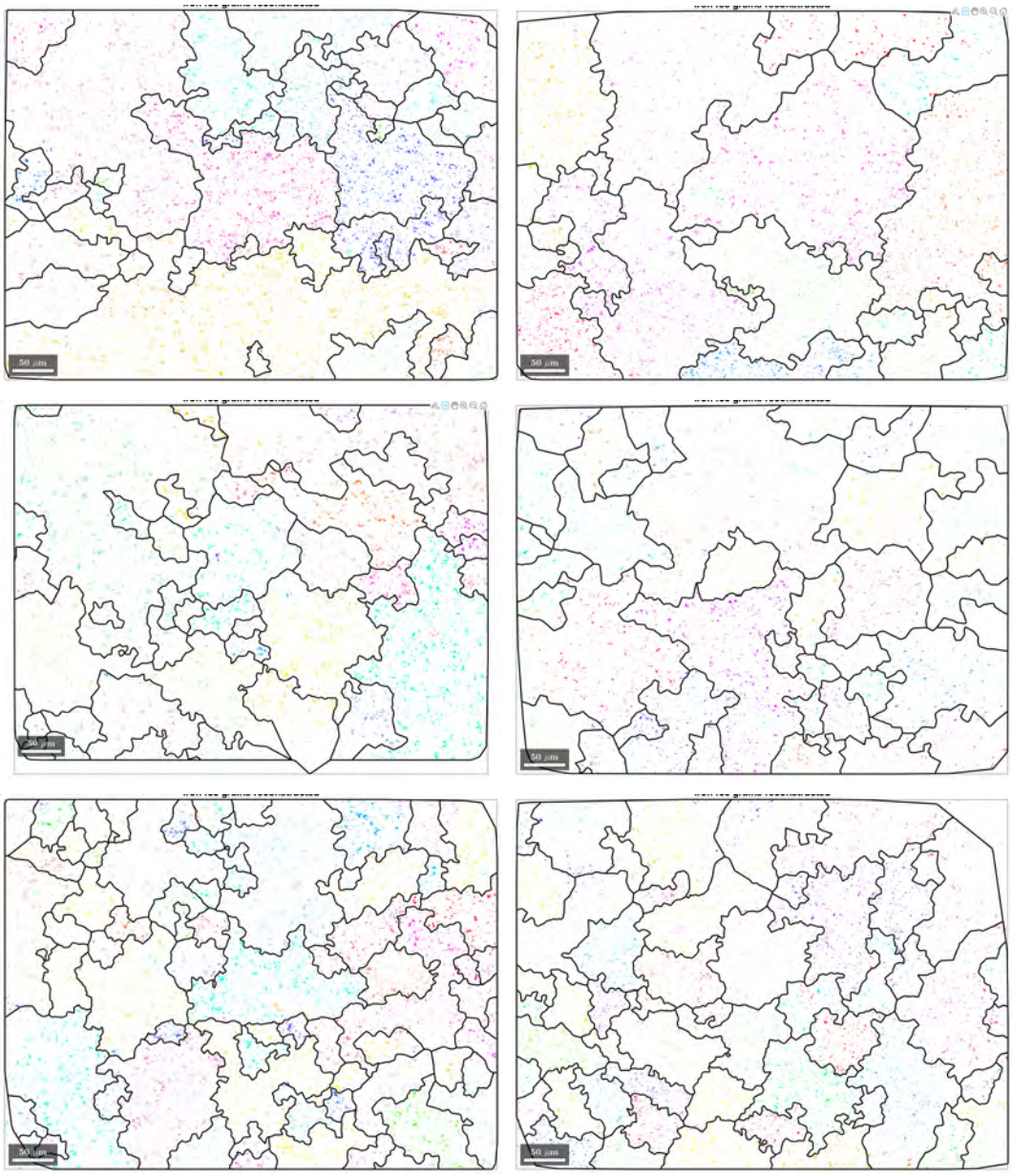

Figure 5.12: EBSD maps coloreed by inverse pole figure (orientation) for the binder phase grains. Comparison between binder phase grain size. Left: 1410°C samples; 02_02 (top), 10_02 (center), 03_02 (bottom). Right: 1500°C samples; 09_03 (top), 02_03 (center), 10_03 (bottom)

5.4 Testing of inserts

5.4.1 Material selection and evaluation

Based on the observations of the structure presented for the samples sintered at 1500°C (see Table 5.1), three materials were observed to have a two-phase structure. Repetitions of these mills were performed (carbon level 2, 3 nd 4) as described in Paragraph 4.3.1 to obtain more powder for further evaluations.
Here, the GT7S100A insert geometry was used and to minimize the problem with porosity high pressing forces were used for these samples. The samples were sintered at both temperatures as previously described. However, they were processed in a different furnace batch, resulting in different sintering charges. Consequently, the first 1410°C sample is expected to be in the η-phase, a result confirmed by LOM observations in the same way as described earlier, as reported in Table 5.7.

Table 5.7: Observed structure for the inserts samples.

		Observed structure	
C content	**Sample code**	**1410°C**	**1500°C**
2	09_i	η-phase	two-phase
3	02_i	two-phase	two-phase
4	10_i	two-phase	two-phase

Results for sample 09_02_i will not be included since this ended up in the η-phase region. Hence, the 1410°C sintering will have samples from two C contents instead of three.
Due to the high pressing forces and the fact that pan dried powders were used, cracks can be observed after sintering on the bottom part of the inserts. Based on this, some of the mechanical property tests needed to be slightly adjusted.
To verify that the inserts pressed with the new powders (which have the same composition as the previous batch) produced comparable microstructural results, the same evaluation procedure described earlier was applied. This included measurements of density and magnetic properties.
Figure 5.13 illustrates the densities of the inserts at different C contents for the two sintering temperatures. Each value represents the average density of three samples corresponding to that C content. For the 1500°C samples, the density increases with C content from the first to the second sample, then decreases from the second to the third. However, the differences are very small, and when the standard deviations are considered (see Appendix A, Table **??**), the materials can be considered to have the same density. Comparing these values with those of the first batch of samples (Figure 5.1), it can be seen that the trends differ. This discrepancy is likely due to the measurement procedure: for the first set of samples, only a single measurement

per sample was performed, whereas the values for the inserts represent an average of three measurements.
For 1410°C sintering, density increases between the two samples, but also in this case, if the standard deviation is taken into account, it can be said that the materials have the same density. The trend is not matched with the first batch of samples.
Further, it can be seen that the densities are comparable for the two sinterings, because the values do not show a large difference, especially if the standard deviation is considered.

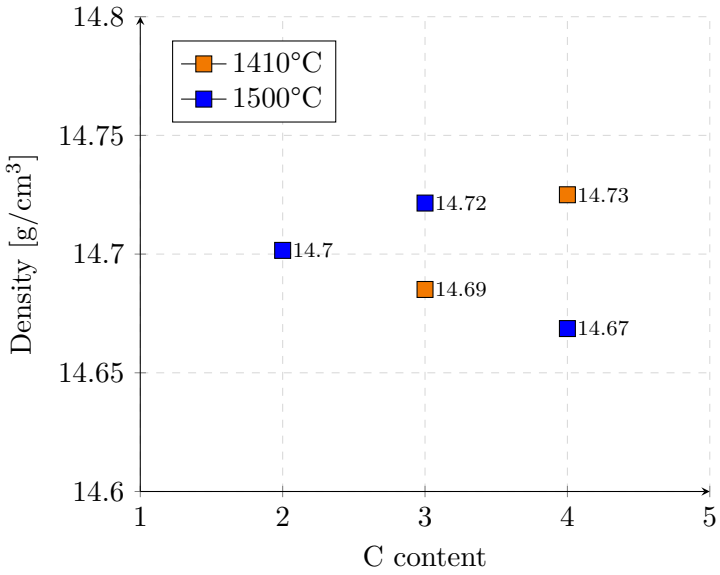

Figure 5.13: Density vs C content for the insert samples.

Figure 5.14 shows the coercivity values for the insert samples, revealing similar trends for both sintering temperatures. For 1500°C sintered samples, coercivity increases from the first to the second sample and then decreases from the second to the third. 1410°C exhibits a comparable increase between its two samples. A difference, however, emerges between the first and second sintering charges: while 1500°C follows the same trend in both charges, 1410°C shows a variation, particularly for the sample with a C level of 4 (see Appendix A, Table A.4 for more details). A discussion and comparison of the Hc between first series with SNUN shaped samples and this second series with insert shaped materials can be found in Appendix C.
A similar pattern is observed for Co-m% in Figure 5.15. In accordance with the SNUN samples, these trends are confirmed for the inserts: for 1500°C sintering, there is an increase in the values, followed by a decrease; the increase is shown also for 1410°C. Since the η-phase - two-phase limit is shifted towards higher C content for 1410°C, a hypothetical sample with C content 5 is expected to show a decrease in Com%, as was shown for the first batch of samples (see Appendix A, Table A.5 for more details).
Table 5.8 reports density, coercivity and Co-m% for the sintering controls for the inserts charges. The Co-m% value for the 1410°C sintering is lower than the 1500°C as already observed in Table 5.2, which means that the atmosphere during 1410°C

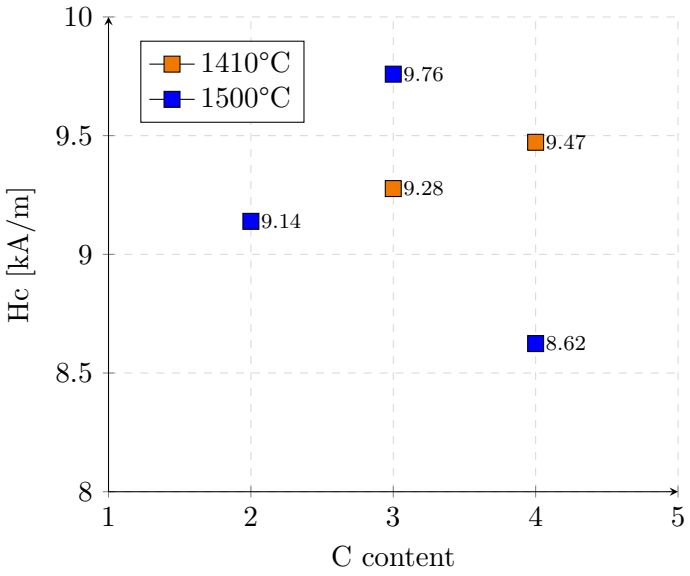

Figure 5.14: Hc vs C content for the inserts samples.

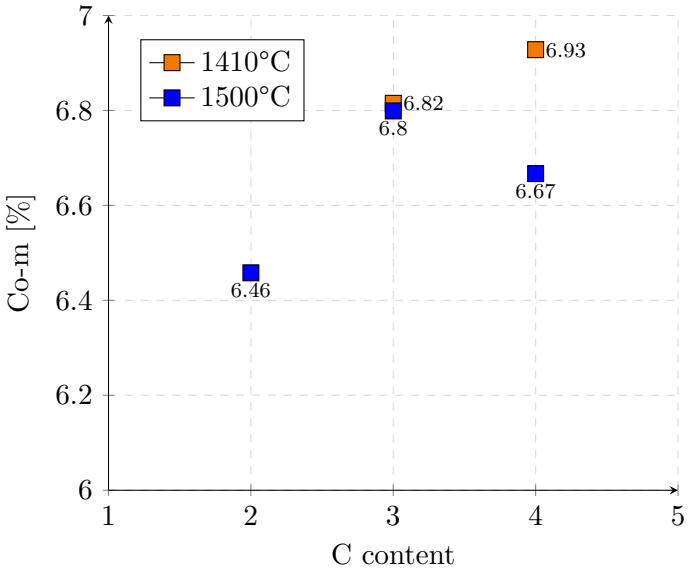

Figure 5.15: Co-m% vs C content for the inserts samples.

sintering is poorer in carbon, thus shifting the two-phase region to higher carbon contents.

Table 5.8: Control samples for the sintering of the inserts: density, coercivity, and magnetic saturation.

Control	**Sintering**	**Density** $[g/cm^3]$	**Hc** $[kA/m]$	**Co-m** [%]
REF_02_i	1410°C	13.1124	11.83	9.011
REF_03_i	1500°C	13.1074	10.11	9.202

5.4.2 Effect of post treatment

After the post-treatment, some samples fractured at the bottom where pre-existing cracks had been observed, due to pressing issues described above. Hence, only data from the top of the inserts will be considered. This does not affect the validity of the hardness mapping results, which is the technique used to evaluate the effect of post treatment. In general, the post-treatment will increase the hardness at affected zones and a difference from the bulk can be achieved. Hence, here the hardness change is of interest.

The effect of the post treatment is mainly confined at this zone at the top edge, while the bulk material keeps its original hardness.

Figure 5.16 shows an example of hardness map. The circles on the map represent the place where the indents were made.

It is confirmed that the effect of post-treatment is mainly on the surfaces layers, while the bulk material keeps the original hardness value. To create these maps, HV3 was used, so the values cannot be compared with the HV20 values measured before. The hardness percentage between surface and bulk was evaluated. These values were extrapolated from the raw data of the map. The hardness value at 6mm from the tip is chosen as the bulk value, thus resolving the problem with crack in the bottom for some inserts, since this part then was excluded.

Table 5.9 reports the percentage change in hardness between the bulk and the surface for the same material subjected to different post-treatment process. It can be seen that different treatments lead to a different percentage change in hardness. This trend is confirmed by the data in the table: the highest ΔHV% is observed for P5, whereas the lowest value is obtained with program P1.

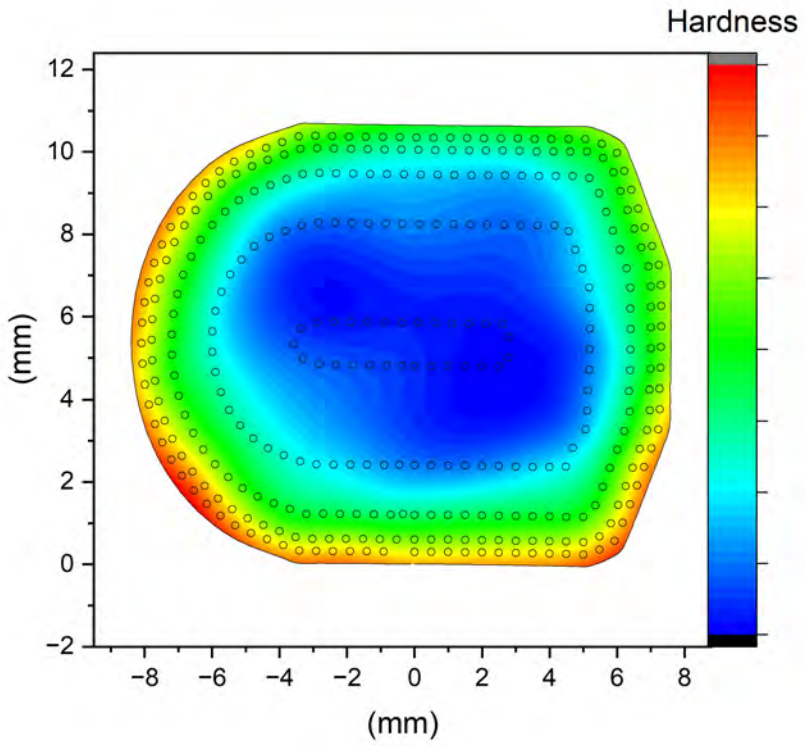

Figure 5.16: Example of hardness distribution map, program P5. The color scale indicates hardness difference across the section.

Table 5.9: Hardness change between surface and bulk. Same composition, different treatment.

Sample: 02_02_i		
Sintering T [°C]	Program	ΔHV [%]
1410	P1	0.613
1410	P2	1.388
1410	P5	2.172

5.4.3 Wear test

Figure 5.17 shows the result of the wear test. The values presented are an average obtained from the two samples used for each composition in the test. For the1410°C samples, higher C content result in less wear. For the 1500°C samples, an increase in C content correlates with higher wear. It can be pointed out that for the first two materials the standard deviation is very low, while for the third material is higher (see Appendix A, Table A.6).
Further research is thus needed to improve the statistics and to fully understand the wear behavior correlation to C content for these materials.

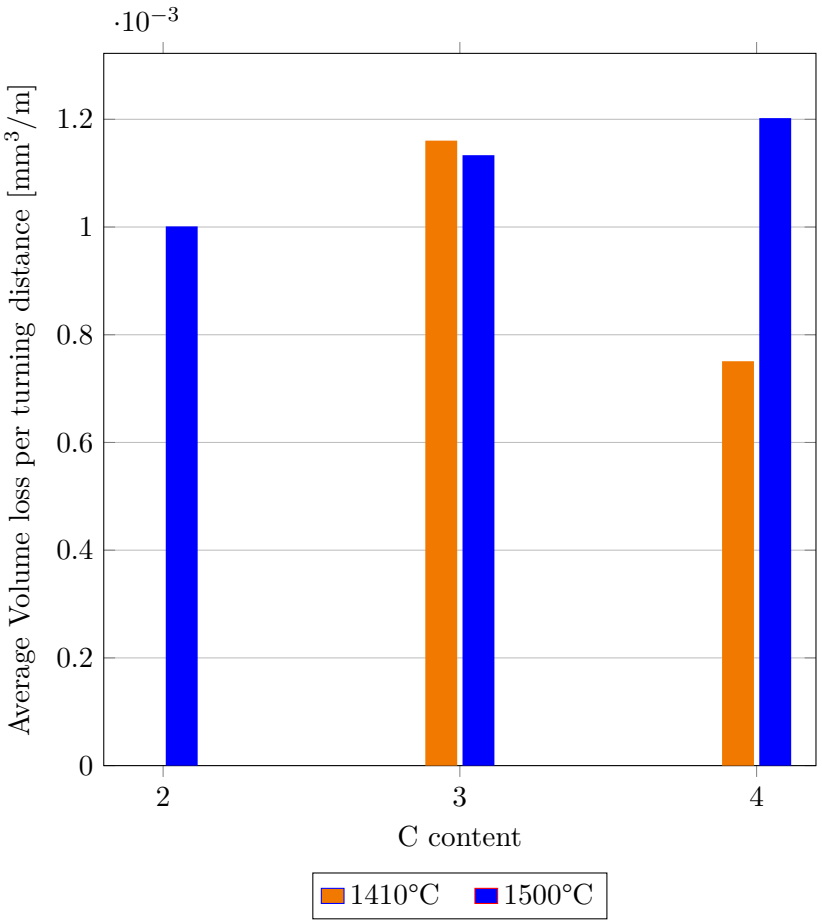

Figure 5.17: Wear test result: Average volume loss vs C level.

Figure 5.18 displays images of the tip from two samples exposed for the wear test: one for a 1410°C sintered sample (left) and one for a 1500°C sample (right). In both cases, darker areas are visible, representing rock fragments adhered to the surface after testing.
These pictures were taken using the stereo microscope and through the software it was possible to measure the area and the diameter of the wear scar. The values are reported in Table 5.10. For every material, the values reported are an average made using the data from two samples. *Area* is the value measured through the software, *Mean D* is the average of the diameters measured through the software and *Calc. area* is the area calculated using *Mean D*. This procedure was followed because the

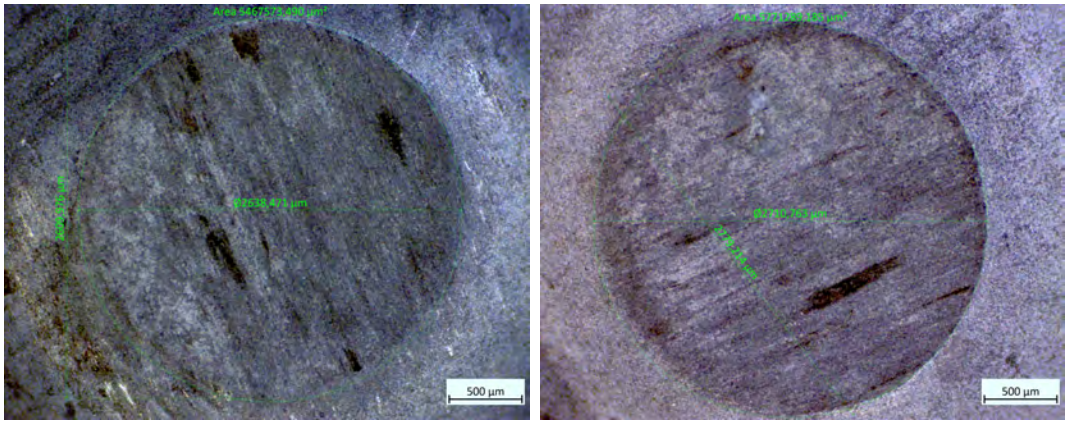

Figure 5.18: Stereo micrographs of the tips from samples exposed to wear test. Left: 10_02_i; right: 10_03_i.

scars do not have a perfect circular shape, thus the values are not accurate, but still can provide an additional element to the understanding of the test. It can be seen that for some samples the difference between the values is not large, while for others it is, probably due to the not perfect circular shape. It can be noted that no clear correlation is observed between volume loss and scar measurements. The lack of trend may be attributed to material inhomogeneities in the rock and to progressive rock consumption during the test. Toller-Nordström [79], however, showed that it is possible to obtain a relation between volume loss and wear scar, for cemented carbides with Fe-based alterative binders. Thus, further investigations can be made on this test.
There are no obvious differences between rock adhesion on the different materials, comparing the stereo images.

Table 5.10: Wear scars measurements and calculations with standard deviation.

Sintering	Sample	Area (mm^2)	Mean D (mm)	Calc. area (mm^2)
1500°C	**09_03**	5.994±0.081	2.790±0.009	6.113±0.039
	02_03	5.811±0.175	2.736±0.007	5.879±0.030
	10_03	5.719±0.074	2.702±0.061	5.736±0.258
1410°C	**02_02**	5.473±0.535	2.647±0.146	5.513±0.609
	10_02	5.473±0.007	2.594±0.042	5.287±0.172

5.4.4 Crush test

The results of the crush test can just be seen as an indication, because only two samples for each composition were tested, so the statistic is poor. Furthermore, those samples already had an internal crack at the bottom (at least this crack was observed

in most of them), which highly affects the test. However, the results show that the fracture energy is increasing with carbon content for 1500°C sintering. This result is encouraging, because it is showing the same trend as for fracture toughness. Indeed, these two properties are related through fracture mechanics principles: fracture energy G_{IC} and fracture toughness K_{IC} are connected by the relation $G_{IC} = \frac{K_{IC}^2}{E'}$, where E' is the effective elastic modulus. This means that an increase in fracture toughness generally corresponds to an increase in fracture energy, provided the elastic properties remain comparable.

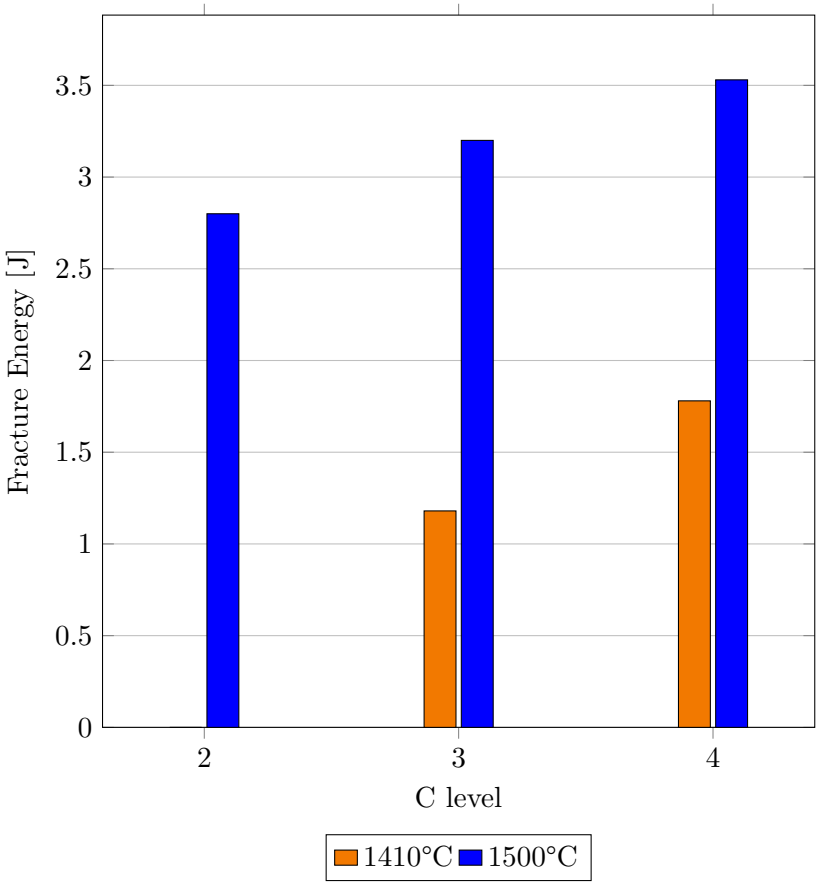

Figure 5.19: Crush test result: Fracture energy vs C level.

Also for 1410°C samples fracture energy increases with carbon content, but the values are extremely low with very high standard deviation (see Appendix A, Table A.7). This is likely due to the fact that samples did not break during the test; the final force registered by the instrument was very low for the first sample, and higher for the second one, but still low compared to the values of the 1500°C samples.

5.5 Hc, WC grain size and hardness relation

According to the theory for Co-based binders, Hc is inversely proportional to WC grain size (see Paragraph 3.2). For 1410°C samples (Figure 5.20), Hc decreases as carbon content increases. For the area weighted average WC grain size (D50) it is increasing between C level 3 and 4, and then it is steady between C level 4 and 5.

The small negligible difference in D50 cannot explain the large difference in Hc.

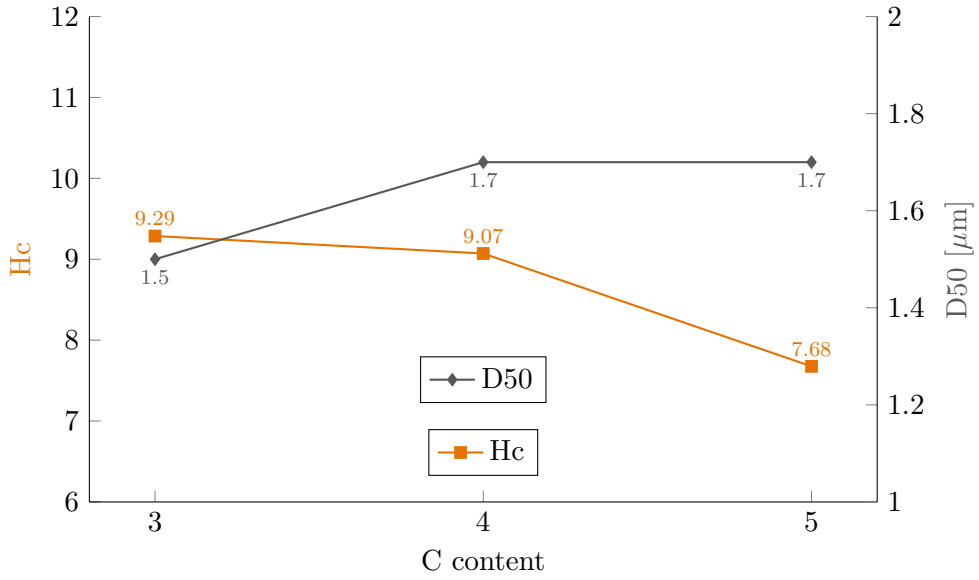

Figure 5.20: Relation between Hc, WC grain size (expressed as D50) and C content, for 1410°C samples.

For 1500°C samples (Figure 5.21), the same pattern is confirmed: D50 can be considered constant and thus the large difference in Hc cannot be explained with just te WC grain size.

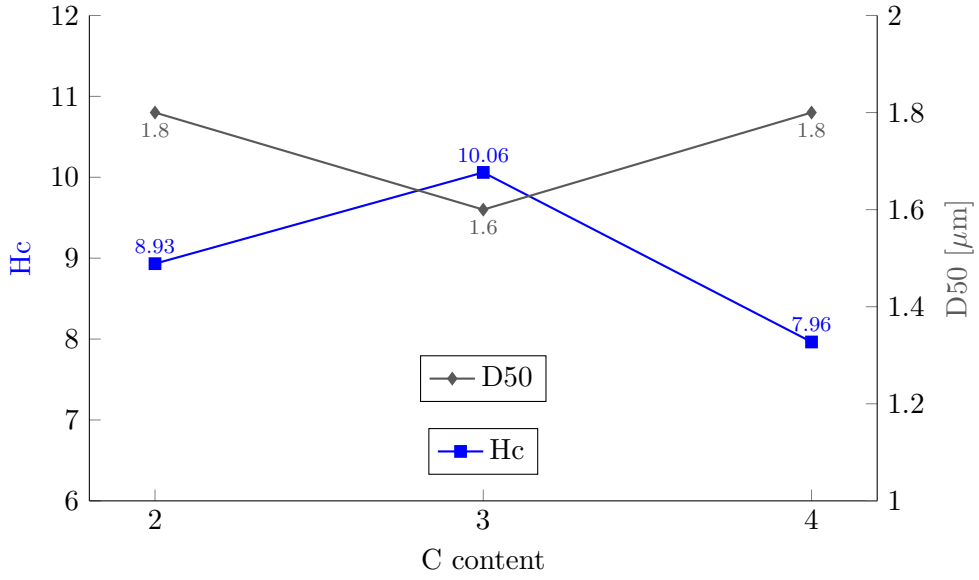

Figure 5.21: Relation between Hc, WC grain size (expressed as D50) and C content, for 1500°C samples.

It is sure that to have a complete picture of the relation between Hc and WC grain size for these materials more data are needed, also to provide a good statistic. This is specially needed for the Hc evaluation where the number of samples was limited. Further studies could explore whether the relationship between Hc and microstructure remains valid beyond the limits of the two-phase structure. As shown in Figure 5.2,

Hc values for samples containing graphite decrease as C content increases. Compared with Co based binders, this trend aligns with expectations, as higher C content typically promotes the formation of larger WC grains. This observation is consistent with the earlier studies showing that high C content favors the growth of larger and more truncated WC grains, as previously discussed. Further investigations could also focus on samples containing the η-phase. Despite their low C content, these samples exhibit low Hc values. Additionally, attention should be given to the shape of the curves and the reason behind the peak occurring at the same C content for both sintering temperatures.

As discussed in previous chapters, microstructure is closely related to mechanical properties; therefore, smaller WC grain sizes are generally associated with higher hardness. The relationship between hardness and grain size is described by the Hall–Petch equation [87], shown in Equation 5.2:

$$H = H_0 + \frac{k}{d^{1/2}} \tag{5.2}$$

where H is the hardness, H_0 is the intrinsic hardness of the material, k is the Hall–Petch constant (material-dependent), and d is the mean grain size. For cemented carbides, the overall hardness can be considered a volume-weighted average of the hardness of WC and the binder phase [88]. Since the constants are highly system-specific, only qualitative considerations based on grain size can be made. An example of calculation is provided in Table 5.11.

Table 5.11: Example of calculation of Hall-Petch WC grain size contribution for 1410°C samples.

Sample	D50 [μm]	$\frac{1}{(D50)^{1/2}}$ [μm$^{-1/2}$]
02_02	1.5	0.82
03_02	1.7	0.77

Depending on the values of H_0 and k, and considering the typical hardness measurement uncertainty of ±30 Vickers, it can be concluded that such small differences in WC grain size have a negligible effect on the overall hardness of the material. Therefore, equal WC grain size agrees with equal hardness.

Chapter 6

Conclusions

This work investigate an alternative binder system based on 50%Fe-25%Ni-25%Co for WC cemented carbides, focusing on the influence of carbon content and sintering temperature on microstructure and properties. The conclusions are summarized as follows:

- The C window was successfully mapped.
- The experimental C window is approximately twice as large as the calculated equilibrium one.
- Despite the theoretical narrow C window, it was possible to achieve 3 compositions within the two-phase structure for both sintering temperatures
- Hc is generally decreasing with increasing C content.
- Co-m% does not change inside the two-phase region; overall Co-m% increases with C content.
- Within the two-phase structure, hardness is not changing, neither with C content nor with sintering temperature.
- Within the two-phase structure, toughness is increasing with C content and with sintering temperature.
- Different analysis methods show differences in evaluated binder fraction.
- WC grain size is independent of C content within the two-phase region. However, increasing the sintering temperature results in a coarser upper tail of the grain size distribution compared with the lower temperature.
- Higher C content resulted to reduce true binder grain size whereas increased sintering temperature promoted true binder grain growth.
- It is possible to achieve different hardness changes using different post-treatment parameters.

- Wear increases with C content for higher sintering temperature; this trend is not observed for lower sintering temperature.
- Fracture energy increases with C content for both sintering temperatures.

6.1 Future work

This thesis aimed to provide a deeper understanding of how C content and sintering temperature influence the microstructure and properties of cemented carbides with an iron-based alternative binder. Nevertheless, several aspects remain unexplored and require further investigation to achieve a more complete understanding of this system.

First, the origin of the coercivity peak observed under both sintering conditions should be clarified. Additionally, the potential existence of empirical mathematical relationships between magnetic properties and alternative binder composition merits examination.

Repetition of mechanical tests, particularly the crush test, is essential to establish a stronger statistical basis for performance evaluation. Microstructural analysis post wear test should also be conducted, with special attention to stress-induced phase transformations, such as the transition from an austenitic to a martensitic binder structure. Furthermore, the interaction between the rock and the material during drilling should be investigated to better understand wear mechanisms.

Finally, further optimization of sintering parameters and binder composition could help expand the carbon window and enhance the robustness of this alternative binder system.

Bibliography

[1] I. Konyashin and B. Ries. “Cemented Carbides”. In: Elsevier, 2022. Chap. 1. DOI: https://doi.org/10.1016/C2019-0-04688-2 (cit. on p. 1).

[2] Hugo M. Ortner, Peter Ettmayer, Hans Kolaska, and Ivi Smid. “The history of the technological progress of hardmetals”. In: *International Journal of Refractory Metals and Hard Materials* 49 (2015), pp. 3–8. DOI: https://doi.org/10.1016/j.ijrmhm.2014.04.016 (cit. on p. 1).

[3] Hugo M. Ortner, Peter Ettmayer, and Hans Kolaska. “The history of the technological progress of hardmetals”. In: *International Journal of Refractory Metals and Hard Materials* 44 (2014), pp. 148–159. DOI: https://doi.org/10.1016/j.ijrmhm.2013.07.014 (cit. on p. 1).

[4] G.S Upadhyaya. “Materials science of cemented carbides — an overview”. In: *Materials & Design* 22.6 (2001), pp. 483–489. DOI: https://doi.org/10.1016/S0261-3069(01)00007-3 (cit. on pp. 1, 10, 11).

[5] *DOE Fundamentals Handbook: Material Science, Volume 1 of 2*. Tech. rep. DOE-HDBK-1017/1-93. Approved for public release; distribution is unlimited. Washington, D.C.: U.S. Department of Energy, 1993. URL: https://www.standards.doe.gov/standards-documents/1000/1017-BHdbk-1993-v1 (cit. on p. 1).

[6] Iowa State University. *Toughness definition*. Accessed on September, 24, 2025. URL: https://www.nde-ed.org/Physics/Materials/Mechanical/Toughness.xhtml (cit. on p. 1).

[7] Daniela Andreina Sandoval Ravotti, Hortensia Melero Correas, and Núria Cinca Luis. “Last decade insights on cemented carbides: A review on alternative binders, new consolidation techniques and advanced characterization”. In: *Eclética Química* 49 (July 2024), e–1529. DOI: 10.26850/1678-4618.eq.v49.2024.e1529. URL: https://revista.iq.unesp.br/ojs/index.php/ecletica/article/view/1529 (cit. on p. 2).

[8] Volkmar Richter, Annegret Potthoff, Wolfgang Pompe, Michael Gelinsky, H. Ikonomidou, Susanne Bastian, Kristin Schirmer, Stefan Scholz, and Jürgen Hofinger. “Evaluation of health risks of nano- and microparticles”. In: *Powder Metallurgy* 51 (Mar. 2008), pp. 8–9. DOI: 10.1179/174329008X286640 (cit. on p. 2).

[9] Pascal Wild, Alain Perdrix, Sylvie Romazini, Jean-Jacques Moulin, and François Pellet. "Lung cancer mortality in a site producing hard metals". In: *Occupational and Environmental Medicine* 57.8 (2000), pp. 568–573. DOI: 10.1136/oem.57.8.568 (cit. on p. 2).

[10] Susanne Bastian et al. "Toxicity of Tungsten Carbide and Cobalt-Doped Tungsten Carbide Nanoparticles in Mammalian Cells in Vitro". In: *Environmental Health Perspectives* 117.4 (2009), pp. 530–536. DOI: 10.1289/ehp.0800121 (cit. on p. 2).

[11] European Commmision. *Critical Raw Materials*. Accessed on September, 18, 2025. URL: https://single-market-economy.ec.europa.eu/sectors/raw-materials/areas-specific-interest/critical-raw-materials_en (cit. on pp. 2, 12).

[12] European Commmision. *REACH enforcement*. Accessed on September, 18, 2025. URL: https://single-market-economy.ec.europa.eu/sectors/chemicals/reach/reach-enforcement_en (cit. on p. 2).

[13] Christopher John Howard Wort. "Applications for Superhard and Ultra-Hard Materials". In: *Microstructure-Property Correlations for Hard, Superhard, and Ultrahard Materials*. Ed. by Valentine Kanyanta. Cham: Springer International Publishing, 2016, pp. 25–74. DOI: 10.1007/978-3-319-29291-5_2 (cit. on p. 2).

[14] José García, Verónica Collado Ciprés, Andreas Blomqvist, and Bartek Kaplan. "Cemented carbide microstructures: a review". In: *International Journal of Refractory Metals and Hard Materials* 80 (2019), pp. 40–68. DOI: https://doi.org/10.1016/j.ijrmhm.2018.12.004 (cit. on pp. 2, 6, 8–10, 12, 18, 19).

[15] Anders Thelin, Jan Qvick, and Gunnar Brandt. "Powder Metallurgy in Sweden 100 years of development". In: Bulls Graphic AB, 2022. Chap. 3-Metal Cutting, pp. 59–81 (cit. on p. 3).

[16] Torbjörn Hartzell, Anders Olsson, Olof Haglund Bengt, Tomas Rotvall, and Susanne Norgren. "Powder Metallurgy in Sweden: 100 Years of Development". In: Bulls Graphic AB, 2022. Chap. 3-Rock Drilling, pp. 40–59 (cit. on p. 3).

[17] Leo Prakash, H. Holleck, F. Thuemmler, and P. Walter. "INFLUENCE OF THE BINDER COMPOSITION ON THE PROPERTIES OF Wc-Fe/Co/Ni CEMENTED CARBIDES." In: *Modern Developments in Powder Metallurgy* 14 (Jan. 1981), pp. 255–268 (cit. on pp. 3, 15, 26).

[18] José García and Wolfgang Strelsky. "Process development and scale up of cemented carbide production". In: Jan. 2010, pp. 235–266. ISBN: 978-3-902655-10-3 (cit. on pp. 5, 6).

[19] Gopal S. Upadhyaya. “3 - Production of Metal and Carbide Powders”. In: *Cemented Tungsten Carbides*. Ed. by Gopal S. Upadhyaya. William Andrew Publishing, 1998, pp. 55–88. DOI: https://doi.org/10.1016/B978-081551417-6.50004-6 (cit. on p. 4).

[20] Thomas A. Wolfe, Thomas J. Jewett, and Raj P. Singh Gaur. “1.06 - Powder Synthesis”. In: *Comprehensive Hard Materials*. Ed. by Vinod K. Sarin. Oxford: Elsevier, 2014, pp. 185–212. DOI: https://doi.org/10.1016/B978-0-08-096527-7.00006-4 (cit. on p. 4).

[21] Pankaj K. Mehrotra. “1.07 - Powder Processing and Green Shaping”. In: *Comprehensive Hard Materials*. Ed. by Vinod K. Sarin. Oxford: Elsevier, 2014, pp. 213–235. DOI: https://doi.org/10.1016/B978-0-08-096527-7.00007-6 (cit. on pp. 5, 6).

[22] Gopal S. Upadhyaya. “4 - Consolidation of Cemented Carbides”. In: *Cemented Tungsten Carbides*. Ed. by Gopal S. Upadhyaya. William Andrew Publishing, 1998, pp. 89–137. ISBN: 978-0-8155-1417-6. DOI: https://doi.org/10.1016/B978-081551417-6.50005-8 (cit. on p. 6).

[23] Oleg D. Neikov, Stanislav S. Naboychenko, Irina B. Murashova, and Nikolay A. Yefimov. “Chapter 23 - Production of Refractory Metal Powders”. In: *Handbook of Non-Ferrous Metal Powders (Second Edition)*. Ed. by Oleg D. Neikov, Stanislav S. Naboychenko, and Nikolay A. Yefimov. Second Edition. Oxford: Elsevier, 2019, pp. 685–755. ISBN: 978-0-08-100543-9. DOI: https://doi.org/10.1016/B978-0-08-100543-9.00023-3 (cit. on p. 6).

[24] Hans-Olof Andrén. “Microstructures of cemented carbides”. In: *Materials Design* 22.6 (2001), pp. 491–498. DOI: https://doi.org/10.1016/S0261-3069(01)00006-1 (cit. on pp. 6, 11).

[25] C.H. Allibert. “Sintering features of cemented carbides WC–Co processed from fine powders”. In: *International Journal of Refractory Metals and Hard Materials* 19.1 (2001), pp. 53–61. DOI: https://doi.org/10.1016/S0263-4368(01)00004-X (cit. on p. 6).

[26] Randall M. German. “1.08 - Consolidation Techniques”. In: *Comprehensive Hard Materials*. Ed. by Vinod K. Sarin. Oxford: Elsevier, 2014, pp. 237–263. DOI: https://doi.org/10.1016/B978-0-08-096527-7.00008-8 (cit. on p. 7).

[27] Z. Zak Fang, Xu Wang, Taegong Ryu, Kyu Sup Hwang, and H.Y. Sohn. “Synthesis, sintering, and mechanical properties of nanocrystalline cemented tungsten carbide – A review”. In: *International Journal of Refractory Metals and Hard Materials* 27.2 (2009), pp. 288–299. DOI: https://doi.org/10.1016/j.ijrmhm.2008.07.011 (cit. on p. 7).

[28] Zeju Weng, Kaixuan Gu, Kaikai Wang, Xuanzhi Liu, Huikun Cai, and Junjie Wang. "Effect of deep cryogenic treatment on the fracture toughness and wear resistance of WC-Co cemented carbides". In: *International Journal of Refractory Metals and Hard Materials* 85 (2019), p. 105059. ISSN: 0263-4368. DOI: https://doi.org/10.1016/j.ijrmhm.2019.105059 (cit. on p. 7).

[29] Chang Ye, Chaoyi Zhang, Jingyi Zhao, and Yalin Dong. "Effects of Post-processing on the Surface Finish, Porosity, Residual Stresses, and Fatigue Performance of Additive Manufactured Metals: A Review". In: *Journal of Materials Engineering and Performance* 30.9 (2021), pp. 6407–6425. ISSN: 1544-1024. DOI: 10.1007/s11665-021-06021-7. URL: https://doi.org/10.1007/s11665-021-06021-7 (cit. on p. 8).

[30] Mingfeng Ke, Lanying Shao, Yuyang Chen, Hengmei Yuan, Jiahuan Wang, Honglin Li, Saurav Goel, Xingsheng Wu, and Binghai Lyu. "Surface pretreatment methods for cemented carbide substrates of the coated cutting tools: A review". In: *Precision Engineering* 96 (2025), pp. 663–691. ISSN: 0141-6359. DOI: https://doi.org/10.1016/j.precisioneng.2025.07.019 (cit. on p. 8).

[31] Eric Bennett, Lewis Lay, Roger Morrell, and Bryan Roebuck. *Microstructural Measurements on Ceramics and Hardmetals*. Measurement Good Practice Guide 21. Updated November 2007. Teddington, Middlesex, UK: National Physical Laboratory, 1997. URL: https://www.npl.co.uk/publications/microstructural-measurements-on-ceramics-and-hardmetals (cit. on p. 8).

[32] Mikhail Slobodyan, Evgeniy Pesterev, and Alexey Markov. "A review of high-energy processing techniques applied for additive manufacturing and surface engineering of cemented carbides and cermets". In: *Journal of Manufacturing Processes* 105 (2023), pp. 124–186. ISSN: 1526-6125. DOI: https://doi.org/10.1016/j.jmapro.2023.09.030 (cit. on p. 9).

[33] A.S. Kurlov and Gusev A.I. "Tungsten carbides and W-C phase diagram". In: *Inorganic materials* 42 (2006). DOI: https://doi.org/10.1134/S0020168506020051 (cit. on p. 9).

[34] Erik Lassner and Wolf-Dieter Schubert. *Tungsten: Properties, Chemistry, Technology of the Element, Alloys, and Chemical Compounds*. New York: Kluwer Academic / Plenum Publishers, 1999. ISBN: 978-0306450538. DOI: 10.1007/978-1-4615-4907-9 (cit. on p. 9).

[35] H. E. Exner. "Physical and chemical nature of cemented carbides". In: *International Metals Reviews* 24.1 (1979), pp. 149–173. DOI: 10.1179/imtr.1979.24.1.149 (cit. on p. 9).

[36] Jonathan Weidow, Sven Johansson, Hans-Olof Andrén, and Göran Wahnström. "Transition Metal Solubilities in WC in Cemented Carbide Materials". In: *Journal of the American Ceramic Society* 94.2 (2010), pp. 605–610. DOI: https://doi.org/10.1111/j.1551-2916.2010.04122.x (cit. on p. 9).

[37] Karin Mannesson, Johan Jeppsson, Annika Borgenstam, and John Ågren. "Carbide grain growth in cemented carbides". In: *Acta Materialia* 59.5 (2011), pp. 1912–1923. ISSN: 1359-6454. DOI: https://doi.org/10.1016/j.actamat.2010.11.056. URL: https://www.sciencedirect.com/science/article/pii/S1359645410008116 (cit. on p. 10).

[38] Young Joon Park, Nong Moon Hwang, and Duk Yong Yoon. "Abnormal growth of faceted (WC) grains in a (Co) liquid matrix". In: *Metallurgical and Materials Transactions A* 27.9 (1996), pp. 2809–2819. DOI: 10.1007/BF02652373 (cit. on p. 10).

[39] tec-science. *Important types of lattice structures*. Accessed: 2025-10-07. May 2018. URL: https://www.tec-science.com/material-science/structure-of-metals/important-types-of-lattice-structures/ (cit. on p. 10).

[40] Martin A. Gren. "Atomic-scale modelling of interfaces in cemented carbides: wetting and strength". PhD thesis. Chalmers University of Technology, 2017 (cit. on p. 10).

[41] Sabine Lay and Jean-Michel Missiaen. "1.03 - Microstructure and Morphology of Hardmetals". In: *Comprehensive Hard Materials*. Ed. by Vinod K. Sarin. Oxford: Elsevier, 2014, pp. 91–120. ISBN: 978-0-08-096528-4. DOI: https://doi.org/10.1016/B978-0-08-096527-7.00003-9 (cit. on pp. 10, 47).

[42] Bernhard Wittmann, Wolf-Dieter Schubert, and Benno Lux. "WC grain growth and grain growth inhibition in nickel and iron binder hardmetals". In: *International Journal of Refractory Metals and Hard Materials* 20.1 (2002), pp. 51–60. ISSN: 0263-4368. DOI: https://doi.org/10.1016/S0263-4368(01)00070-1 (cit. on pp. 10, 12, 13).

[43] T. Nishizawa and K. Ishida. "The Co (Cobalt) system". In: *Bulletin of Alloy Phase Diagrams* 4.4 (1983), pp. 387–390. ISSN: 0197-0216. DOI: 10.1007/BF02868089 (cit. on p. 10).

[44] Gopal S. Upadhyaya. "Cemented Tungsten Carbides". In: *Cemented Tungsten Carbides*. Westwood, NJ: William Andrew Publishing, 1998. ISBN: 978-0-8155-1417-6. DOI: https://doi.org/10.1016/B978-081551417-6.50001-0 (cit. on p. 11).

[45] Martin Walbrühl, David Linder, John Ågren, and Annika Borgenstam. "Diffusion modeling in cemented carbides: Solubility assessment for Co, Fe and Ni binder systems". In: *International Journal of Refractory Metals and Hard Materials* 68 (2017), pp. 41–48. ISSN: 0263-4368. DOI: https://doi.org/10.1016/j.ijrmhm.2017.06.006 (cit. on p. 11).

[46] J. O. Andersson, T. Helander, L. Höglund, P. F. Shi, and B. Sundman. "Thermo-Calc and DICTRA, Computational tools for materials science". In: *Calphad* 26 (2002). Software used: Thermo-Calc version 2025a, pp. 273–312. DOI: 10.1016/S0364-5916(02)00037-8. URL: https://doi.org/10.1016/S0364-5916(02)00037-8 (cit. on pp. 11, 13, 14, 16, 26, 27).

[47] S. Farag, I. Konyashin, and B. Ries. "The influence of grain growth inhibitors on the microstructure and properties of submicron, ultrafine and nano-structured hardmetals – A review". In: *International Journal of Refractory Metals and Hard Materials* 77 (2018), pp. 12–30. ISSN: 0263-4368. DOI: https://doi.org/10.1016/j.ijrmhm.2018.07.003 (cit. on p. 12).

[48] William E. Gent, Grace M. Busse, and Kurt Z. House. "The predicted persistence of cobalt in lithium-ion batteries". In: *Nature Energy* 7.12 (2022), pp. 1132–1143. ISSN: 2058-7546. DOI: 10.1038/s41560-022-01129-z. URL: https://doi.org/10.1038/s41560-022-01129-z (cit. on p. 12).

[49] *Report on Carcinogens Monograph on Cobalt and Cobalt Compounds that Release Cobalt Ions In Vivo*. Tech. rep. RoC Monograph 06. Reasonably anticipated to be a human carcinogen. National Toxicology Program (NTP), U.S. Department of Health and Human Services, 2016. URL: https://doi.org/10.22427/ROC-MGRAPH-06 (cit. on p. 12).

[50] Zoé Roulon. "Effect of binder on sintering and microstructure of cemented carbides". Doctoral Thesis. Université Grenoble Alpes, 2019. URL: https://theses.hal.science/tel-02442394/ (cit. on p. 12).

[51] Zoé Roulon, Jean-Michel Missiaen, and Sabine Lay. "Shrinkage and microstructure evolution during sintering of cemented carbides with alternative binders". In: *International Journal of Refractory Metals and Hard Materials* 101 (2021), p. 105665. ISSN: 0263-4368. DOI: https://doi.org/10.1016/j.ijrmhm.2021.105665 (cit. on pp. 12, 13).

[52] C.M. Fernandes and A.M.R. Senos. "Cemented carbide phase diagrams: A review". In: *International Journal of Refractory Metals and Hard Materials* 29.4 (2011), pp. 405–418. ISSN: 0263-4368. DOI: https://doi.org/10.1016/j.ijrmhm.2011.02.004 (cit. on p. 12).

[53] R. K. Viswanadham and P. G. Lindquist. "Transformation-toughening in cemented carbides: Part I. Binder composition control". In: *Metallurgical Transactions A* 18.12 (1987), pp. 2163–2173. ISSN: 2379-0180. DOI: 10.1007/BF02647089. URL: https://doi.org/10.1007/BF02647089 (cit. on pp. 12, 14).

[54] Björn Uhrenius, Henri Pastor, and Emmanuel Pauty. "On the composition of Fe-Ni-Co-WC-based cemented carbides". In: *International Journal of Refractory Metals and Hard Materials* 15.1 (1997), pp. 139–149. ISSN: 0263-4368. DOI: https://doi.org/10.1016/S0263-4368(96)00023-6 (cit. on pp. 13–15).

[55] V.A Tracey. "Nickel in hardmetals". In: *International Journal of Refractory Metals and Hard Materials* 11.3 (1992), pp. 137–149. ISSN: 0263-4368. DOI: https://doi.org/10.1016/0263-4368(92)90056-8 (cit. on p. 13).

[56] T. W. Penrice. "Alternative binders for hard metals". In: *Journal of Materials Shaping Technology* 5.1 (1987), pp. 35–39. ISSN: 0931-704X. DOI: 10.1007/BF02833684 (cit. on p. 13).

[57] I. Konyashin. "Approaching the 100th anniversary of the Hardmetal invention: From first WC-Co samples towards modern advanced Hardmetal grades". In: *International Journal of Refractory Metals and Hard Materials* 111 (2023), p. 106113. ISSN: 0263-4368. DOI: https://doi.org/10.1016/j.ijrmhm.2023.106113. URL: https://www.sciencedirect.com/science/article/pii/S0263436823000136 (cit. on p. 14).

[58] W.D. Schubert, M. Fugger, B. Wittmann, and R. Useldinger. "Aspects of sintering of cemented carbides with Fe-based binders". In: *International Journal of Refractory Metals and Hard Materials* 49 (2015). Special Issue: International Conference on the Science of Hard Materials – 10, pp. 110–123. ISSN: 0263-4368. DOI: https://doi.org/10.1016/j.ijrmhm.2014.07.028. URL: https://www.sciencedirect.com/science/article/pii/S0263436814001735 (cit. on pp. 14, 15).

[59] Chunxin Liu. "Alternative Binder Phases for WC Cemented Carbides". Master's Thesis. KTH Royal Institute of Technology, 2015. URL: https://www.researchgate.net/publication/324138110_ALTERNATIVE_BINDER_PHASES_FOR_WC_CEMENTED_CARBIDES (cit. on pp. 14, 15, 46).

[60] Gerhard Gille, J Bredthauer, B Gries, B Mende, and W Heinrich. "Advanced and new grades of WC and binder powder – their properties and application". In: *International Journal of Refractory Metals and Hard Materials* 18.2 (2000), pp. 87–102. ISSN: 0263-4368. DOI: https://doi.org/10.1016/S0263-4368(00)00002-0. URL: https://www.sciencedirect.com/science/article/pii/S0263436800000020 (cit. on p. 14).

[61] Yang Gao, Bing-Hui Luo, Ke-Jian He, Wen-Wen Zhang, and Zhen-Hai Bai. "Effect of Fe/Ni ratio on the microstructure and properties of WC-Fe-Ni-Co cemented carbides". In: *Ceramics International* 44.2 (2018), pp. 2030–2041. ISSN: 0272-8842. DOI: https://doi.org/10.1016/j.ceramint.2017.10.148. URL: https://www.sciencedirect.com/science/article/pii/S0272884217323544 (cit. on p. 15).

[62] J. Heinrichs, S. Norgren, S. Jacobson, K. Yvell, and M. Olsson. "Influence of binder metal on wear initiation of cemented carbides in sliding contact with granite". In: *Wear* 470-471 (2021), p. 203645. ISSN: 0043-1648. DOI: https://doi.org/10.1016/j.wear.2021.203645. URL: https://www.sciencedirect.com/science/article/pii/S004316482100034X (cit. on p. 15).

[63] Andrew J. Ruys. "8 - Cemented carbides and cermets". In: *Metal-Reinforced Ceramics*. Ed. by Andrew J. Ruys. Elsevier Series in Advanced Ceramic Materials. Woodhead Publishing, 2021, pp. 285–325. ISBN: 978-0-08-102869-8. DOI: https://doi.org/10.1016/B978-0-08-102869-8.00008-2. URL: https://www.sciencedirect.com/science/article/pii/B9780081028698000082 (cit. on p. 15).

[64] Lisa Toller-Nordström. "Insights into wear and deformation of alternative binder hardmetals". PhD thesis. Uppsala Universitet, 2019. URL: https://www.diva-portal.org/smash/record.jsf?pid=diva2:1362889 (cit. on p. 16).

[65] David Linder. "Towards Computational Materials Design and Upscaling of Alternative Binder Cemented Carbides". PhD thesis. Stockholm, Sweden: KTH Royal Institute of Technology, 2020. ISBN: 978-91-7873-433-7. URL: https://www.diva-portal.org/smash/get/diva2:1388274/FULLTEXT01.pdf (cit. on pp. 17, 18).

[66] Padmakumar Muthuswamy and D. Dinakaran. "Evaluation of mechanical and metallurgical properties of cryo-treated tungsten carbide with 25% cobalt". In: *Materials Today: Proceedings* 43 (2021). International Conference on Nano-electronics, Nanophotonics, Nanomaterials, Nanobioscience Nanotechnology, pp. 3463–3469. ISSN: 2214-7853. DOI: https://doi.org/10.1016/j.matpr.2020.09.374. URL: https://www.sciencedirect.com/science/article/pii/S2214785320370905 (cit. on p. 18).

[67] R. van der Merwe and N. Sacks. "Effect of TaC and TiC on the friction and dry sliding wear of WC–6wt.% Co cemented carbides against steel counterfaces". In: *International Journal of Refractory Metals and Hard Materials* 41 (2013), pp. 94–102. ISSN: 0263-4368. DOI: https://doi.org/10.1016/j.ijrmhm.2013.02.009. URL: https://www.sciencedirect.com/science/article/pii/S0263436813000437 (cit. on p. 18).

[68] David Linder, Ziyong Hou, Ruiwen Xie, Peter Hedström, Valter Ström, Erik Holmström, and Annika Borgenstam. "A comparative study of microstructure and magnetic properties of a NiFe cemented carbide: Influence of carbon content". In: *International Journal of Refractory Metals and Hard Materials* 80 (2019), pp. 181–187. ISSN: 0263-4368. DOI: https://doi.org/10.1016/j.ijrmhm.2019.01.014. URL: https://www.sciencedirect.com/science/article/pii/S0263436818308229 (cit. on pp. 18, 37).

[69] Joseph I. Goldstein, Dale E. Newbury, Joseph R. Michael, Nicholas W. M. Ritchie, John Henry J. Scott, and David C. Joy. *Scanning Electron Microscopy and X-Ray Microanalysis*. 4th ed. New York, NY: Springer, 2018. ISBN: 978-1-4939-6674-5. DOI: 10.1007/978-1-4939-6676-9 (cit. on p. 21).

[70] Wikipedia. *Scanning electron microscope*. Accessed on October, 14, 2025. URL: https://en.wikipedia.org/wiki/Scanning_electron_microscope (cit. on pp. 21, 22).

[71] Laura J. Powers. "Materials Analysis and Failure Analysis". In: *Encyclopedia of Forensic Sciences, Third Edition (Third Edition)*. Ed. by Max M. Houck. Third Edition. Oxford: Elsevier, 2023, pp. 485–502. ISBN: 978-0-12-823678-9. DOI: https://doi.org/10.1016/B978-0-12-823677-2.00258-0 (cit. on p. 21).

[72] Oxford Instruments. *How does EBSD work?* Accessed on October, 17, 2025. URL: https://www.ebsd.com/ebsd-for-beginners/how-does-ebsd-work (cit. on p. 22).

[73] Oxford Instruments. *Automated EBSD*. Accessed on October, 17, 2025. URL: https://www.ebsd.com/ebsd-for-beginners/automated-ebsd (cit. on p. 22).

[74] Oxford Instruments. *EBSD applications*. Accessed on October, 17, 2025. URL: https://www.ebsd.com/ebsd-for-beginners/ebsd-applications (cit. on p. 22).

[75] Wikipedia. *Electron Back-Scattered Diffraction*. Accessed on October, 17, 2025. URL: https://en.wikipedia.org/wiki/Electron_backscatter_diffraction# (cit. on p. 23).

[76] NPL. *Hardness testing*. Accessed on October,21, 2025. URL: https://www.npl.co.uk/products-services/advanced-materials/hardness-testing?_gl=1*ulo5bz*_up*MQ..*_ga*MTg0ODc2MDU0Ni4xNzYxMDQ2MDgy*_ga_9FQZYXXRX7*czE3NjEwNDYwODEkbzEkZzAkdDE3NjEwNDYwODEkajYwJGwwJGgw (cit. on p. 23).

[77] Wikipedia. *Palmqvist method*. Accessed on October, 22, 2025. URL: https://en.wikipedia.org/wiki/Palmqvist_method (cit. on p. 24).

[78] B. Roebuck, E. Bennet, L. Lay, and R. Morrell. *Fracture Toughness of Advanced Ceramics*. Tech. rep. CMMT(A) 90. National Physical Laboratory, 2008. URL: https://eprintspublications.npl.co.uk/1566/1/mgpg9.pdf (cit. on p. 24).

[79] L. Toller-Nordström, S. Sten, M. Kritikos, S. Norgren, A. Borgenstam, and I. Borgh. "Wear properties of cemented carbides with new binder solutions for rock drilling inserts". In: *Wear* 570 (2025). 25th International Conference on Wear of Materials, p. 205909. ISSN: 0043-1648. DOI: https://doi.org/10.1016/j.wear.2025.205909. URL: https://www.sciencedirect.com/science/article/pii/S0043164825001784 (cit. on pp. 25, 56).

[80] Xiaokun Yuan and Yuan Ji. "Characterization of grain boundary character distribution in cemented carbides via a stereological method". In: *Processing and Application of Ceramics* 16 (Jan. 2022), pp. 341–350. DOI: 10.2298/PAC2204341Y (cit. on p. 31).

[81] Johannes Schindelin et al. "Fiji: an open-source platform for biological-image analysis". In: *Nature Methods* 9.7 (2012), pp. 676–682. DOI: 10.1038/nmeth.2019 (cit. on p. 32).

[82] The MathWorks Inc. *MATLAB R2024b*. Version R2024b. Natick, Massachusetts, 2024. URL: https://www.mathworks.com/products/matlab.html (cit. on p. 33).

[83] Ralf Hielscher and Helmut Schaeben. "A novel pole figure inversion method: Specification of the MTEX algorithm". In: *Journal of Applied Crystallography* 41 (2008), pp. 1024–1037. DOI: 10.1107/S0021889808030112 (cit. on p. 33).

[84] T. Persson and M. Schwind. "Correlation of WC Grain Size Distribution to Hardness and Coercivity". In: *18th Plansee Seminar*. Reutte, Austria: Plansee SE, 2013 (cit. on p. 45).

[85] Z. Roulon, J.M. Missiaen, and S. Lay. "Carbide grain growth in cemented carbides sintered with alternative binders". In: *International Journal of Refractory Metals and Hard Materials* 86 (2020), p. 105088. ISSN: 0263-4368. DOI: https://doi.org/10.1016/j.ijrmhm.2019.105088. URL: https://www.sciencedirect.com/science/article/pii/S0263436819304664 (cit. on p. 46).

[86] Olivia Danielsson. "Effect of Carbon Activity on Microstructure Evolution in WC–Ni Cemented Carbides". Degree Project in Materials Design and Engineering, Second Cycle, 30 credits. MA thesis. Stockholm, Sweden: KTH Royal Institute of Technology, 2018 (cit. on p. 47).

[87] Cheng Qian, Kun Li, Xue-yi Guo, Bin Liu, Zheng-yi Long, and Yong Liu. "Effect of WC grain size on mechanical properties and microstructures of cemented carbide with medium entropy alloy Co-Ni-Fe binder". In: *Journal of Central South University* 27.4 (2020), pp. 1146–1157. ISSN: 2227-5223. DOI: 10.1007/s11771-020-4355-5. URL: https://doi.org/10.1007/s11771-020-4355-5 (cit. on p. 59).

[88] Satyanarayana V. Emani, Chuanlong Wang, Leon L. Shaw, and Zheng Chen. "On the hardness of submicrometer-sized WC–Co materials". In: *Materials Science and Engineering: A* 628 (2015), pp. 98–103. ISSN: 0921-5093. DOI: https://doi.org/10.1016/j.msea.2014.12.106. URL: https://www.sciencedirect.com/science/article/pii/S0921509314016177 (cit. on p. 59).

Appendix A

Appendix A

Table A.1: Hardness values with standard deviation.

	1410°C		1500°C	
C content	**HV20**	**St.Dev.**	**HV20**	**St.Dev.**
1	1342	69	1354	17
2	1377	5	1360	7
3	1396	7	1404	8
4	1380	5	1382	3
5	1382	7	1356	5
6	1299	41	1310	17
7	1237	17	1238	5
8	1220	7	1210	7

Table A.2: Toughness values with standard deviation.

	1410°C		**1500°C**	
C content	**Toughness**	**St.Dev.**	**Toughness**	**St.Dev.**
1	1.025	0.019	1.019	0.022
2	1.000	0.017	1.110	0.026
3	1.028	0.019	1.209	0.061
4	1.163	0.045	1.457	0.078
5	1.301	0.051	1.631	0.187
6	1.414	0.096	1.726	0.124
7	1.428	0.074	1.518	0.094
8	1.490	0.070	1.478	0.071

Note: Each toughness value was normalized by dividing by the reference toughness. The associated standard deviations were calculated using full uncertainty propagation, such that the uncertainty of both the original measurement and the reference value contribute to the final normalized standard deviation.

Table A.3: Average density and standard deviation for the inserts sintered at different temperatures.

Sintering	**Sample**	**Density (avg.)**	**St.Dev.**
1410°C	02_02_i	14,69	0,03
	10_02_i	14,73	0,03
1500°C	09_03_i	14,70	0,02
	02_03_i	14,72	0,03
	10_03_i	14,67	0,03

Note: Average of three samples for each composition.

Table A.4: Average coercivity (Hc) with standard deviation.

Sintering T	**Sample**	**Hc** $[kA/m]$	**St.Dev.**
1410°C	02_02_i	9.277	0.006
	10_02_i	9.472	0.022
1500°C	09_03_i	9.139	0.025
	02_03_i	9.759	0.010
	10_03_i	8.624	0.013

Note: Average of three samples for each composition.

Table A.5: Average Co-m% with standard deviation.

Sintering T	Sample	Co-m%	St.Dev.
1410°C	02_02_i	6.185	0.004
	10_02_i	6.928	0.035
1500°C	09_03_i	6.458	0.020
	02_03_i	6.799	0.009
	10_03_i	6.667	0.025

Note: Average of three samples for each composition.

Table A.6: Average volume loss per turning distance $[mm^3/m]$ and standard deviation from the wear test.

Sintering	Sample	Volume loss (avg.)	St.Dev.
1410°C	02_02_i	0,00116	0,00012
	10_02_i	0,00075	0,00016
1500°C	09_03_i	0,00100	0,00001
	02_03_i	0,00113	0,00001
	10_03_i	0,00120	0,00031

Note: Average of two samples for each composition.

Table A.7: Average fracture energy [J] and standard deviation.

Sintering	Sample	Fracture energy (avg.)	St.Dev.
1410°C	02_02_i	1,18	1,47
	10_02_i	1,78	2,32
1500°C	09_03_i	2,80	1,41
	02_03_i	3,20	0,01
	10_03_i	3,53	0,35

Note: Average of two samples for each composition.

Appendix B

Appendix B

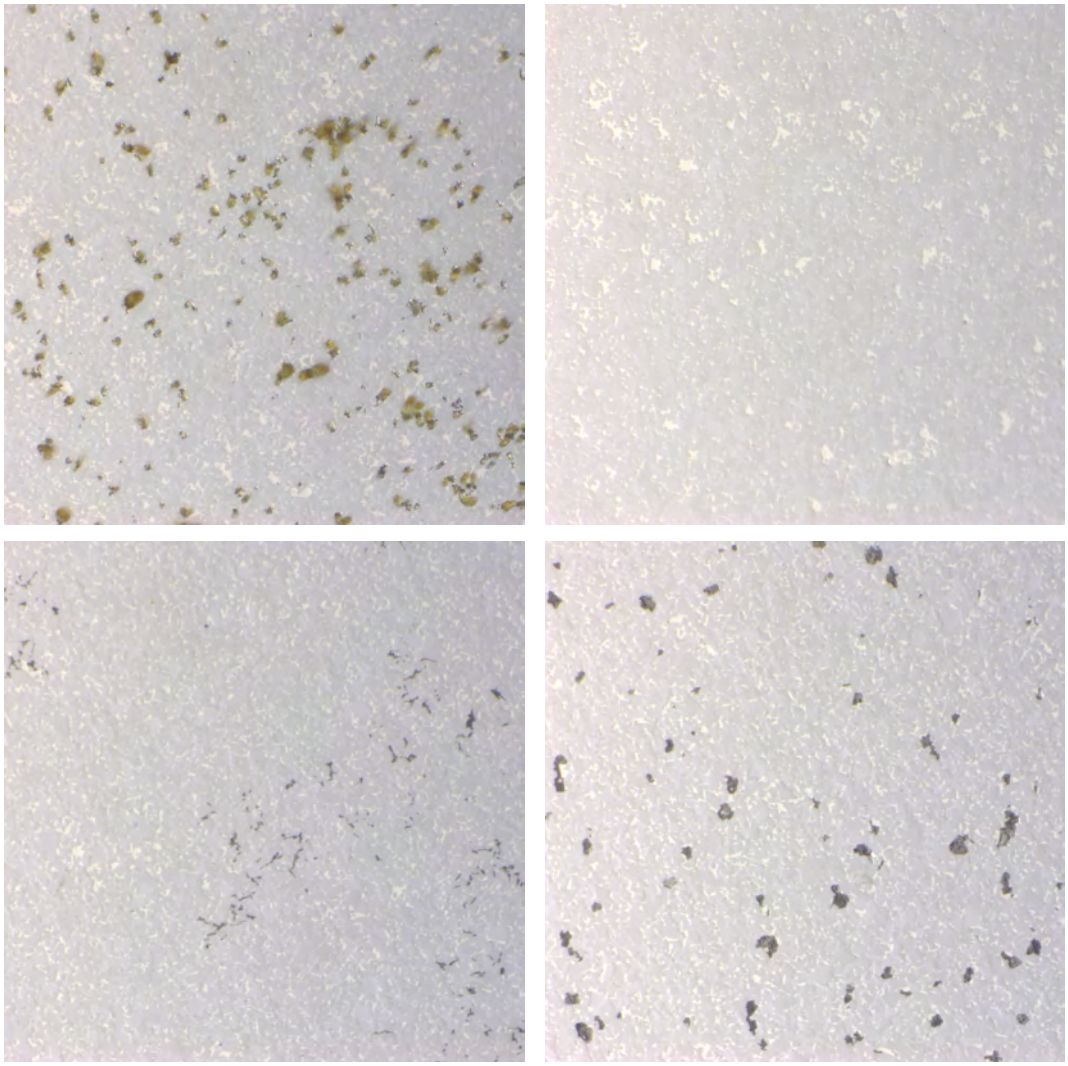

Figure B.1: Observed structures. First row: on the left η-phase in yellow; on the right two-phase structure. Second row: flaked graphite (left) and nodular graphite (right).

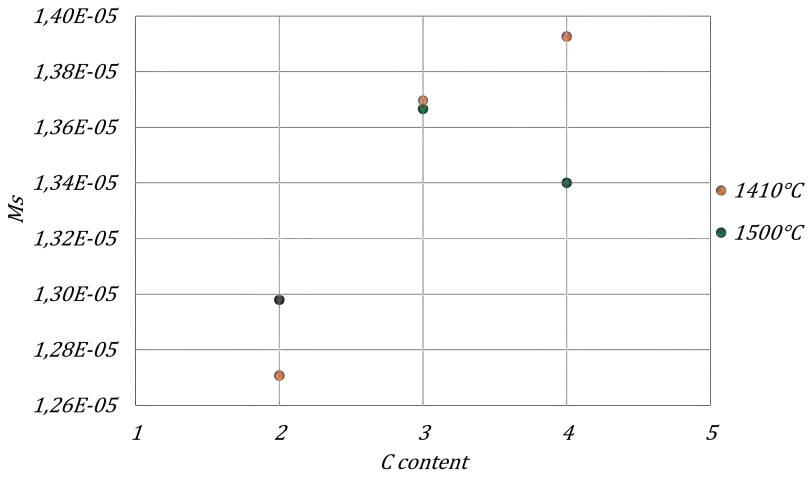

Figure B.2: Magnetic saturation (Ms) vs C content

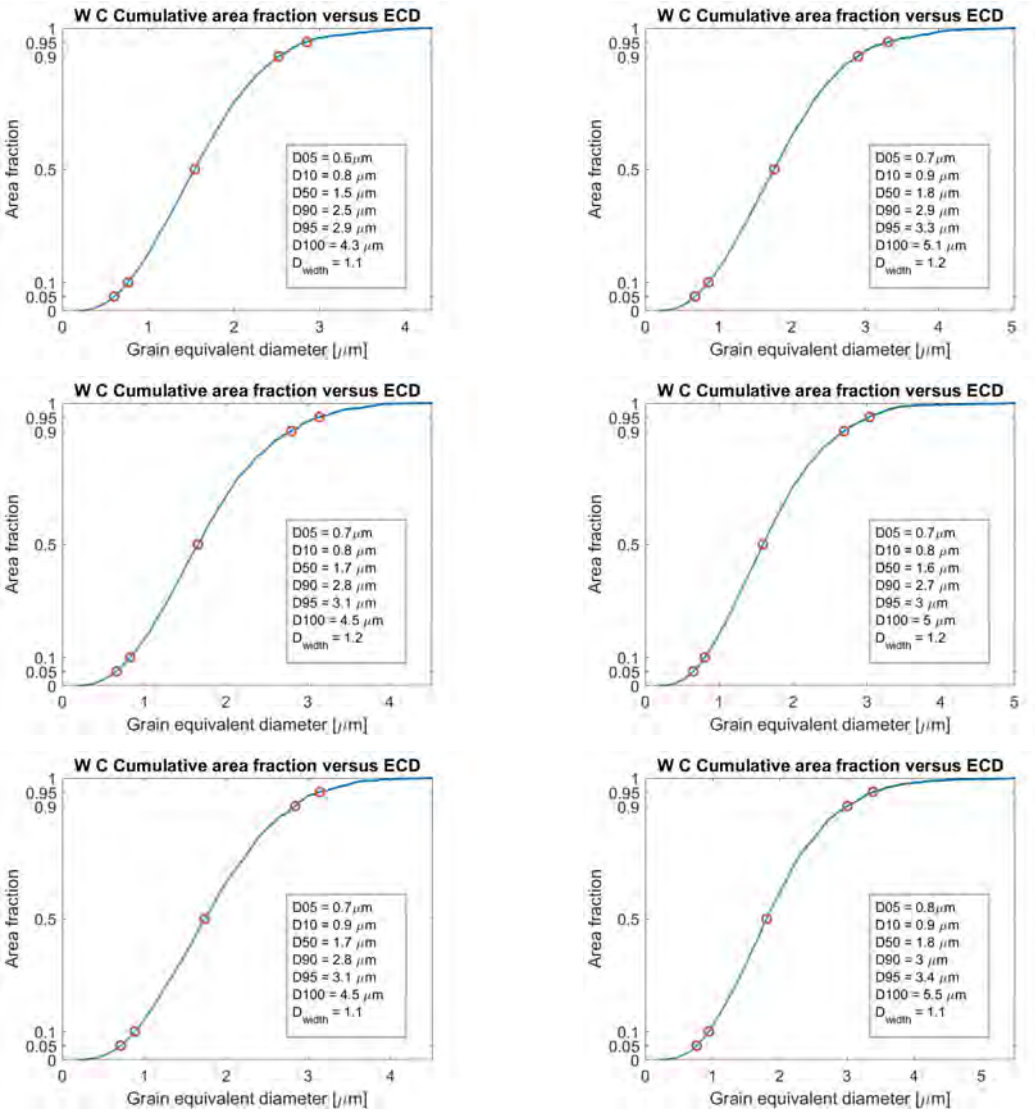

Figure B.3: Comparison between WC cumulative curves. Left: 1410°C samples; 02_02 (top), 10_02 (center), 03_02 (bottom). Right: 1500°C samples; 09_03 (top), 02_03 (center), 10_03 (bottom)

Figure B.4: True binder grain maps for 1410°C samples: 02_02 (top), 10_02 (center), 03_02 (bottom).

Appendix C

Appendix C

C.1 Hc: comparison between different sintering trials

Figure C.1 illustrates the Hc values for both the inserts and the SNUN samples sintered at same temperature, enabling a comparison of the results and assessing whether repeating the same process at different times can yield variations. For the samples sintered using 1500°C, the overall curve shape is consistent across both series; however, the SNUN samples exhibit greater variability in Hc values.
In the 1410°C series, the inserts show a trend where increasing C content corresponds to higher Hc values. Conversely, for the SNUN samples in the same series, the last diamond displays a lower Hc value compared to the middle one. The samples having C content 3 shoe the same Hc value.

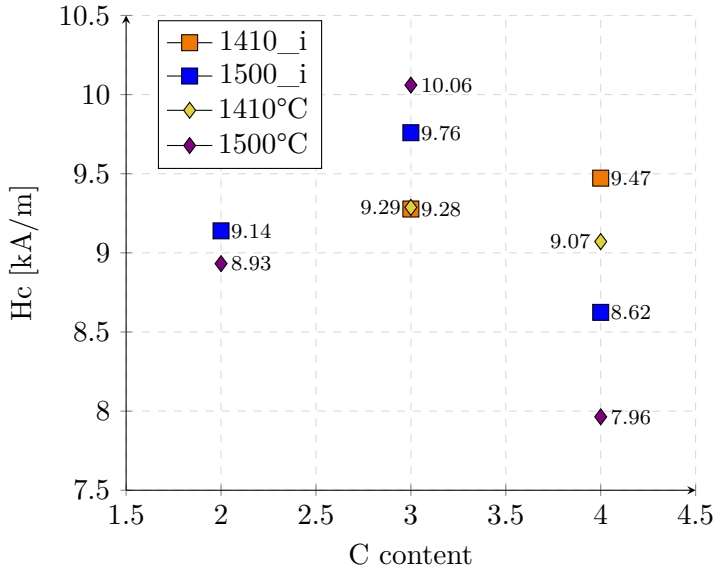

Figure C.1: Hc vs C content: comparison between inserts and SNUNs.